International Journal of Nanomedicine

Dovepress
Taylor & Francis Group

Open Access Full Text Article

ORIGINAL RESEARCH

Transferrin-Functionalized Conjugated Polymer Nanoparticles for Enhanced Photodynamic Therapy of Glioblastoma

Matías Daniel Caverzan[1,2], Bruno Agustín Cesca[3], Rodrigo Emiliano Palacios[1], Carlos Alberto Chesta[1], Luis Exequiel Ibarra[3]

[1]Department of Chemistry, Institute for Research in Energy Technologies and Advanced Materials (IITEMA), National University of Río Cuarto (UNRC) and National Scientific and Technical Research Council (CONICET), Río Cuarto, Argentina; [2]Department of Animal Pathology, Faculty of Agronomy and Veterinary Medicine, National University of Río Cuarto (UNRC), Río Cuarto, Argentina; [3]Department of Molecular Biology, Institute of Environmental Biotechnology and Health (INBIAS), National University of Río Cuarto (UNRC) and National Scientific and Technical Research Council (CONICET), Río Cuarto, Argentina

Correspondence: Luis Exequiel Ibarra, Department of Molecular Biology, Institute of Environmental Biotechnology and Health (INBIAS), National University of Río Cuarto (UNRC) and National Scientific and Technical Research Council (CONICET), Río Cuarto, Argentina, Email libarra@exa.unrc.edu.ar

---

Purpose: Glioblastoma (GBM) remains one of the most lethal primary brain tumors due to its highly infiltrative nature, pronounced intratumoral heterogeneity, and the restrictive blood–brain barrier (BBB), which severely limit the efficacy of conventional therapies. Photodynamic therapy (PDT) offers a spatially and temporally controllable treatment modality; however, its clinical translation for GBM is hindered by insufficient tumor selectivity and suboptimal photosensitizer delivery to intracranial lesions. The purpose of this study was to develop and preclinically evaluate transferrin-functionalized conjugated polymer nanoparticles (CPNs) as a receptor-targeted nanoplatform to enhance BBB traversal, tumor cell uptake, and photodynamic therapeutic efficacy in GBM.

Methods: F8BT-based CPNs doped with platinum(II) octaethylporphyrin (PtOEP) and stabilized with poly(styrene-co-maleic anhydride) (PSMA) were synthesized by controlled nanoprecipitation and covalently conjugated to holo-transferrin (holo-Tf) using EDC/NHS chemistry. Nanoparticles were characterized by dynamic light scattering, zeta potential, UV–visible and fluorescence spectroscopy, transmission electron microscopy, electrophoretic mobility, and protein quantification assays. Cellular uptake, receptor specificity, and photodynamic cytotoxicity were evaluated in GBM cell lines. Therapeutic efficacy was further assessed in an orthotopic U87MG-tdiRFP glioblastoma mouse model.

Results: Holo-Tf functionalization increased nanoparticle hydrodynamic diameter, reduced surface charge magnitude, and introduced a protein-specific absorbance feature, while preserving colloidal stability and optical properties. Protein quantification assays confirmed retention of more than 70% of the input holo-Tf. In vitro, holo-Tf CPNs showed significantly enhanced uptake in TfR-high U87MG cells compared with non-functionalized CPNs (42% vs 18% nanoparticle-positive cells at 1 h; gMFI 211 vs 73 at 4 h), which was reduced by excess free holo-Tf, indicating receptor-mediated uptake. PDT mediated by holo-Tf CPNs produced greater phototoxicity in vitro and, in vivo, reduced tumor fluorescence and prolonged survival relative to controls.

Conclusion: Transferrin functionalization enhances receptor-directed delivery and PDT efficacy of conjugated polymer nanoparticles in GBM, supporting their further optimization and translational development.

Keywords: theranostic nanoplatforms, conjugated polymer nanoparticles, holo-transferrin, orthotopic glioma model, light-activated cancer therapy, active targeting

---

Introduction

Glioblastoma (GBM) remains the most aggressive and lethal primary brain tumor in adults, characterized by diffuse infiltrative growth, pronounced intratumoral heterogeneity, and a unique capacity to evade standard multimodal therapies.[1] Current standard of care (maximal safe resection followed by radiotherapy and temozolomide) yields limited

https://doi.org/10.2147/IJN.S592688
Received: 30 December 2025
Accepted: 13 May 2026
Published: 20 May 2026

Graphical Abstract

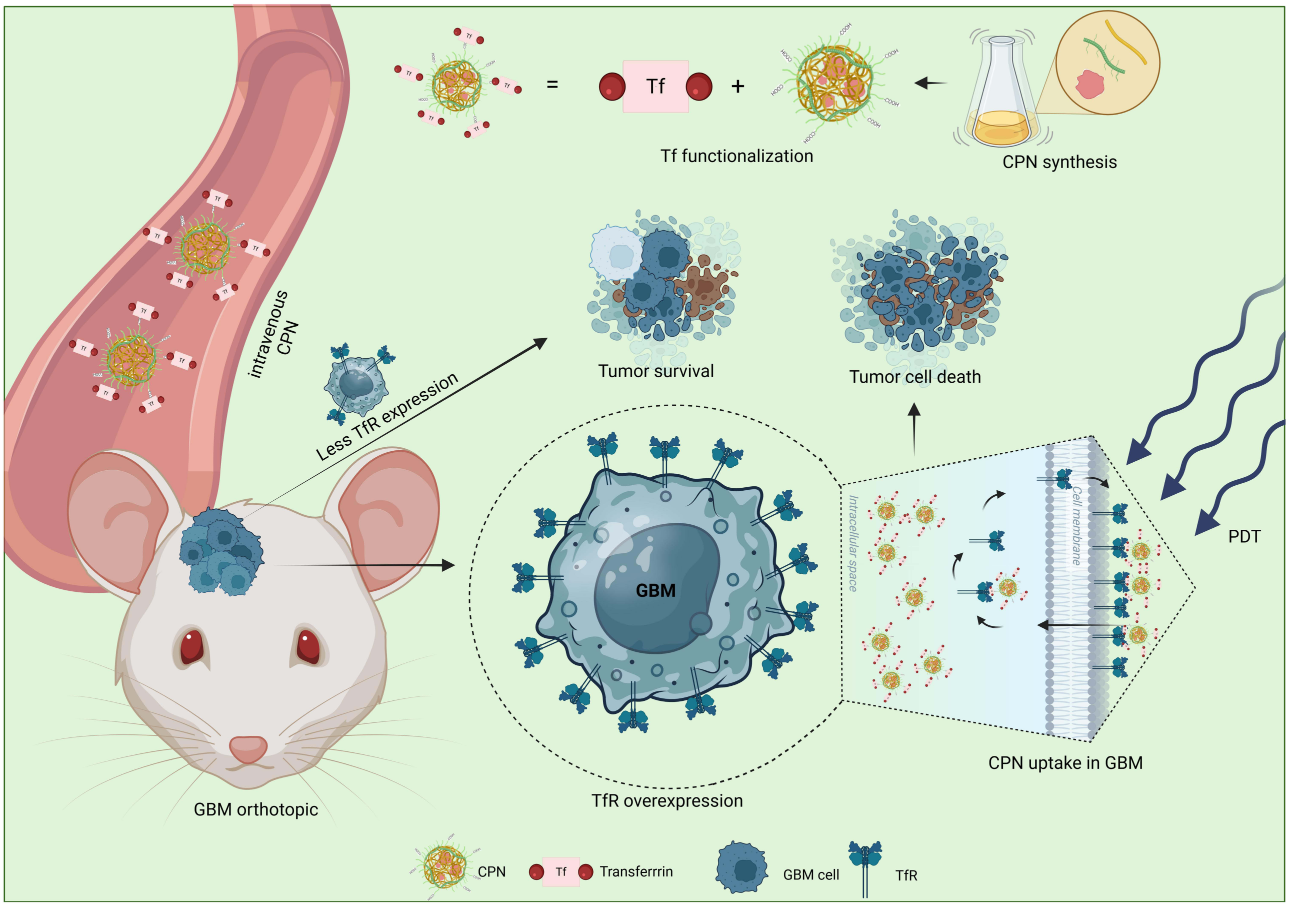

median survival and is frequently compromised by the blood-brain barrier (BBB), poor intratumoral drug penetration, and resistance mechanisms intrinsic to GBM cells.[2] These challenges motivate development of alternative, localized therapeutic strategies that combine high spatial selectivity with the capacity for molecular targeting.

Photodynamic therapy (PDT) is an attractive adjunct or alternative modality for GBM because it enables local generation of cytotoxic reactive oxygen species (ROS) upon light activation of a photosensitizer (PS), thereby allowing spatially confined tumor ablation with minimal systemic exposure.[3–5] Nevertheless, translation of PDT in neuro-oncology has been hindered by the physicochemical limitations of many PSs (hydrophobicity, aggregation, poor photostability), inadequate tumor selectivity, and limited tissue penetration of activating light.[6,7] Moreover, the heterogeneous expression of therapeutic targets within GBM, combined with the restrictive transport across the BBB, underscores the need for delivery platforms capable of enhancing PS performance while ensuring selective accumulation within tumor tissue.

Conjugated polymer nanoparticles (CPNs) combine intense light-harvesting, antenna effect, high photostability, tunable emission, and facile incorporation of hydrophobic PS, making them an attractive class of theranostic nanomaterials for PDT.[8–10] In clinical settings, several PS such as porphyrins, chlorins, and phthalocyanines have already demonstrated therapeutic potential and have been approved for PDT in different oncological indications, highlighting the translational relevance of PS-based strategies. However, many of these molecules suffer from poor aqueous solubility, aggregation, and suboptimal tumor selectivity, which can limit their therapeutic performance.[11] Nanostructured systems such as CPNs have therefore emerged as versatile photoactive nanoplatforms in which hydrophobic PS can be incorporated within the conjugated polymer matrix. Owing to their strong light-harvesting properties and donor–acceptor electronic interactions, CPNs can act as energy-transfer antennas that enhance PS excitation and consequently increase ROS generation upon light activation. When engineered as polymer-stabilized nanoassemblies such as F8BT-based CPNs doped with porphyrin derivatives and colloidally stabilized with amphiphilic copolymers, these nanoparticles can afford strong singlet-oxygen generation, and a platform amenable to surface functionalization.[12,13] Nevertheless, despite their promising photophysical properties and encouraging preclinical results, CPN-based systems still face several challenges, including limited clinical validation, potential variability in biodistribution and clearance profiles, and the need for improved targeting strategies to achieve selective tumor accumulation.[3,14]

Importantly, CPNs based on poly(9,9-dioctylfluorene-alt-benzothiadiazole) F8BT and metallated porphyrins have already undergone toxicological preclinical evaluation, demonstrating safety profiles consistent with translational development. In our recent comprehensive study, platinum(II) porphyrin–doped F8BT CPNs exhibited excellent colloidal stability in clinically relevant infusion media. Moreover, the absence of overt systemic toxicity, together with favorable biodistribution characterized by predominant hepatic and splenic clearance and rapid blood elimination kinetics, provides encouraging evidence that the F8BT CPN platform may achieve a therapeutic alternative compatible with future clinical translation.[15]

Conjugation of targeting ligands to the nanoparticle surface is a straightforward strategy to enhance selective uptake by tumor cells.[16,17] The transferrin receptor 1 (TfR1, CD71) is highly relevant as a GBM target due to its frequently overexpression in malignant glioma cells relative to normal brain tissue, mediates receptor-mediated transcytosis across the BBB, and has been exploited clinically for targeted delivery.[18–20] This receptor, involved in transporting iron into the cell, is markedly overexpressed in GBM cells due to their high proliferation rate and increased metabolic demands.[21] Its limited expression in healthy tissues makes it an attractive therapeutic target for the design of targeted nanoparticles that enable greater tumor specificity and a reduction of systemic adverse effects.[22]

Decorating CPNs with holo-transferrin (holo-Tf), the diferric (iron-saturated) form of transferrin that binds TfR1 with high affinity and enables receptor-mediated iron uptake, can therefore serve a dual function by improving tumor selectivity through TfR-mediated endocytosis while also facilitating transport across endothelial barriers such as the BBB. This strategy preserves the intrinsic photophysical capabilities of conjugated polymers while introducing an active targeting mechanism that may enhance therapeutic selectivity in the GBM microenvironment. In this study, we introduce a targeted conjugated polymer nanoplatform that integrates the light-harvesting properties of F8BT-based CPNs with TfR–mediated targeting to improve the delivery and therapeutic performance of PDT in GBM. We present the design, physicochemical characterization, and preclinical evaluation of holo-Tf–conjugated CPNs as a multifunctional nanoplatform for GBM PDT. Specifically, we investigate ligand conjugation efficiency, nanoparticle physicochemical properties, and receptor-dependent uptake across GBM cell lines with differential TfR1 expression. Furthermore, we demonstrate in vivo intracerebral accumulation and therapeutic efficacy of the targeted nanoplatform in an orthotopic GBM mouse model. Collectively, these results provide a proof-of-concept for combining receptor-targeted delivery with the unique photophysical properties of CPNs to overcome key limitations in GBM PDT.

Materials and Methods

Materials

CPNs were prepared using a commercially available conjugated polymer (CP) poly((9,9-dioctylfluorenyl-2,7-diyl)-co-(1,4-benzo[2,1′,3]-thiadiazole)) (F8BT, Mn = 115,000 g·mol^{-1}, and a polydispersity index of 3.2 (American Dye Source Inc., Canada). F8BT-based CPNs were synthesized employing an amphiphilic stabilizer poly(styrene-co-maleic anhydride) (PSMA; 68% styrene, average molecular weight ≈ 1700 g·mol^{-1} (Sigma-Aldrich, St. Louis, MO, USA). Formulations were prepared either doped or undoped with platinum(II) octaethylporphyrin (PtOEP, >95%, Frontier Scientific, Logan, UT, USA). Tetrahydrofuran (THF, HPLC grade, Cicarelli, Santa Fe, Argentina) was refluxed for 5 h with potassium hydroxide pellets (KOH, pro-analysis grade, Taurus) and subsequently distilled. Milli-Q water obtained from a Milli-Q® purification system (Millipore, Merck) with a resistivity of 18.2 MΩ·cm at 25 °C and free of organic contaminants, ions and particles was used for all aqueous solutions and procedures requiring high purity.

Human holo-transferrin (holo-Tf, 97%, MW 76 kDA, Sigma Aldrich, St. Louis, MO, USA) was dissolved in 20 mM HEPES buffer, pH 7.2 (MW 238.3, Sigma Aldrich), at a concentration of 1 mg·mL^{-1}. 1-Ethyl-3-(3-dimethylaminopropyl) carbodiimide hydrochloride (EDC, Sigma Aldrich, St. Louis, MO, USA) was dissolved in 20 mM HEPES buffer, pH 7.2, at a concentration of 5 mg·mL^{-1}. N-hydroxysuccinimide (NHS, Sigma Aldrich, St. Louis, MO, USA) was dissolved in 20 mM HEPES buffer, pH 7.2, also at a concentration of 5 mg·mL^{-1}.

Cells and Animals

Three GBM cell lines (U87MG, ATCC® HTB-14™; T98G, ATCC® CRL-1690™; and M059K, ATCC® CRL-2365™) and one normal human kidney cell line (HEK-293, ATCC® CRL-1573™) were used. For the assays of orthotopic GBM development in animal models, U87MG-tdiRFP cells were generated via plasmid transfection with polyethyleneimine (PEI) utilizing the plasmid pCAG-H2BtdiRFP-IP (Addgene plasmid # 47884) to express the tandem dimer red fluorescent protein (tdiRFP), followed by the selection of clones exhibiting constitutive protein expression upon puromycin exposure at 10 µg/mL over a duration of 28 days. All human tumor and non-tumor cell lines were cultivated in Dulbecco's modified Eagle's medium (DMEM, Sigma-Aldrich, MO, USA) augmented with 10% v/v fetal bovine serum (FBS), 1% v/v glutamine (GlutaMAX™ 100x), and 1% v/v antibiotics (penicillin 10,000 units/mL – streptomycin 10,000 µg/mL). Cells were cultured in a humidified incubator with 5% CO_2 at 37°C.

Adult Non-Obese Diabetic, Severe Combined Immunodeficient (NOD/SCID) mice were used, from the animal facility of the Faculty of Exact, Physical, Chemical and Natural Sciences of the National University of Río Cuarto (UNRC). The mice were housed in plastic cages with bedding in a ventilated, temperature-controlled, and standardized sterile animal room. They were maintained under a 12/12 h light/dark cycle, with food and water available ad libitum. All procedures, in accordance with the International Guidelines for the Care and Use of Laboratory Animals, were approved by the Research Ethics Committee (CoEdI) of the UNRC (code 300/21).

Preparation of F8BT-Based Conjugated Polymer Nanoparticles and Holo-Transferrin Surface Functionalization

CPNs were synthesized using a previously reported nanoprecipitation method.[12,15] Briefly, a stock solution of the CP F8BT was prepared by dissolving the polymer in fresh THF to a final concentration of approximately 500 mg·L^{-1}. The solution was filtered through a 0.2 µm pore size PTFE membrane syringe filter (Iso-Disc, Sigma-Aldrich, St. Louis, MO, USA) to eliminate any undissolved particulated matter. The concentration of the filtered solution was re-determined by UV-visible spectroscopy using a known absorption coefficient in THF at 456 nm (45.4 g^{-1} L cm^{-1}). Separately, stock solutions of PSMA (2 g·L^{-1}) and PtOEP (0.25 g·L^{-1}) in THF were also prepared. The three solutions were subsequently combined to achieve final concentrations of 50 mg·L^{-1} for F8BT, 10 mg·L^{-1} for PSMA, and 5 mg·L^{-1} for PtOEP in THF. A 10 mL volume of the F8BT/PSMA/PtOEP solution was rapidly injected into 20 mL of Milli-Q water under continuous sonication (Arcano PS-30A, Buenos Aires, Argentina), and the resulting dispersion was sonicated for an additional 10 minutes. Subsequently, THF and a fraction of the water were removed by reduced-pressure evaporation using a rotary evaporator, concentrating the nanoparticle dispersion to a final volume of approximately 8 mL. The resulting suspension was then filtered through a cellulose acetate membrane with a pore size of 0.2 µm (25 mm, gamma-sterile, Micron Separation Inc., Westborough, MA, USA) to eliminate large aggregates. The volume of the filtered dispersion was adjusted to 10 mL by the addition of Milli-Q water, and the final CPN concentration was recalculated and expressed in terms of F8BT mass concentration (mg·L^{-1}), using the previously established absorption coefficient for pure F8BT CPNs in water.[8] Finally, various stock batches of CPN suspensions were formulated with a final F8BT content of 50–100 mg·L^{-1} depending on experimental requirement. Two F8BT-based CPNs were synthetized for further holo-Tf conjugation and subsequent experiments: F8BT stabilized with PSMA for cell labeling purposes (designated as F8BT CPNs); and those using F8BT, PSMA and PtOEP for PDT treatment due to its increased photodynamic effect (designated as F8BT-PtOEP CPNs).[10]

To facilitate clarity throughout the manuscript, non-functionalized nanoparticles are referred to as F8BT CPNs or F8BT–PtOEP CPNs, whereas holo-Tf–functionalized nanoparticles are denoted as F8BT–Tf CPNs or F8BT–PtOEP–Tf CPNs, depending on the nanoparticle core composition. For simplicity, these formulations are collectively referred to as CPNs throughout the manuscript unless otherwise specified.

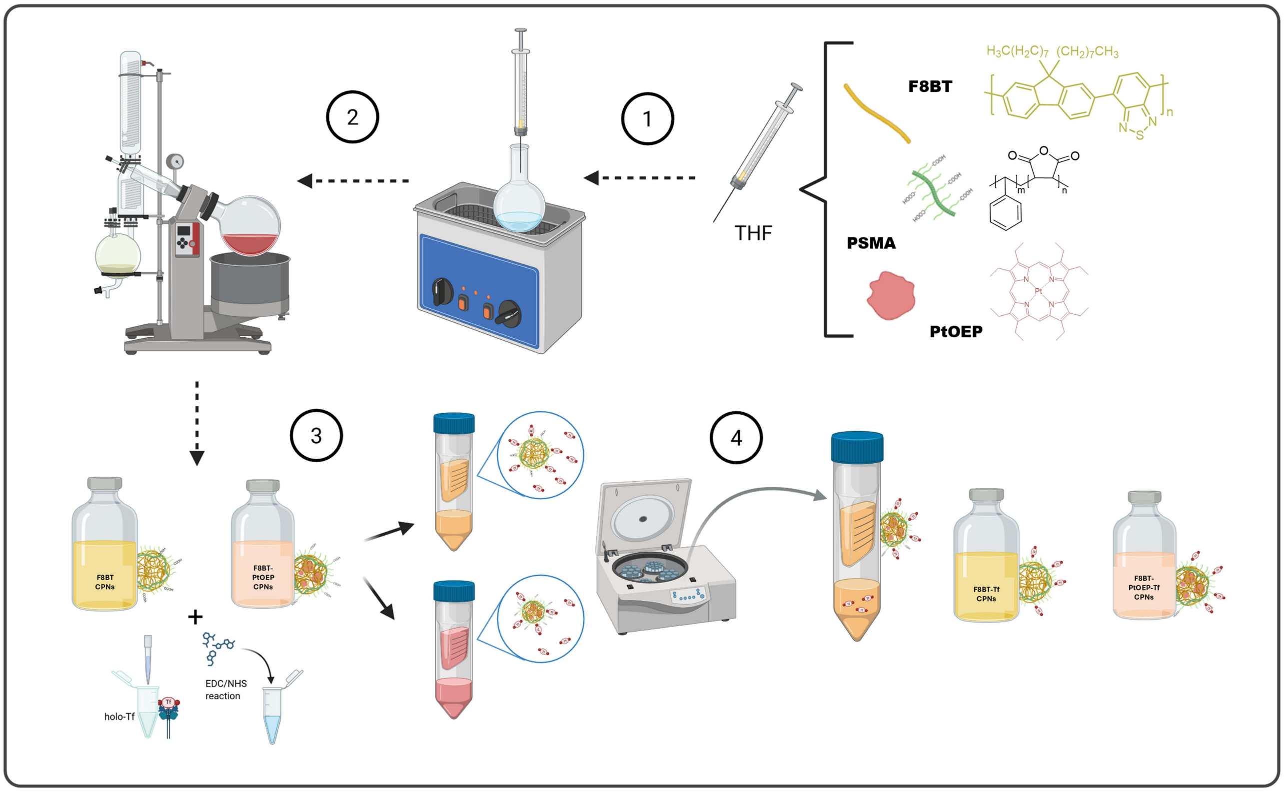

Figure 1 Schematic representation of the synthesis and functionalization workflow of F8BT-based CPNs. (1) *Controlled nanoprecipitation*: F8BT, PSMA, and optionally PtOEP were dissolved in THF and rapidly injected into Milli-Q water under sonication to form polymeric nanoaggregates. (2) *Solvent removal and purification*: THF was evaporated using a rotary evaporator, and crude dispersions were further purified. (3) *Surface functionalization*: F8BT CPNs and F8BT-PtOEP CPNs were reacted with holo-Tf via EDC/NHS-mediated carbodiimide coupling to generate holo-Tf-decorated CPNs. (4) *Post-reaction cleanup*: Functionalized and non-functionalized CPNs were washed and concentrated by centrifugation, yielding final formulations of F8BT CPNs and F8BT-PtOEP CPNs, with or without holo-Tf. Created in BioRender.

Aiming to conjugate F8BT CPNs or F8BT-PtOEP CPNs surface with holo-Tf, sterile vials were employed containing each type of CPNs (1 mL, 50 mg·L^{-1}), with the addition of 20 µL of 1 M HEPES buffer (pH 7.2); 20 µL of EDC solution and followed by 10 µL of NHS. Finally, 60 µL of holo-Tf (1 mg·mL^{-1}) was added and mixing was conducted through vortexing. The solutions were incubated for 24 hours in darkness at 4°C with continuous stirring. The elimination of free holo-Tf molecules was conducted through filtration utilizing VIVASPIN TURBO 100kDa MWCO (Sartorius, Göttingen, Germany) concentrator tubes featuring a regenerated cellulose membrane. Centrifugation was performed at 800 × g and 4 °C for three successive cycles, replacing the supernatant with 500 µL of fresh Milli-Q water after each step to thoroughly wash the CPN dispersions and removed exceeded protein (Figure 1).

Evaluation of Physicochemical Characteristics of Functionalized CPNs

The physicochemical characterization of CPNs (F8BT CPNs and F8BT-PtOEP CPNs) was performed using dynamic light scattering (DLS) and electrophoretic light scattering (Zeta-Sizer Nano ZS90, Malvern Instruments, UK) to determine the mean hydrodynamic diameter (d_h), polydispersity index (PDI), and zeta potential (ζ). Optical properties were evaluated by UV–visible absorption spectroscopy (HP 8452A Diode Array Spectrophotometer, Agilent Technologies Inc., Santa Clara, CA, USA) and fluorescence emission spectroscopy (Fluoromax-4, Horiba Scientific, Edison, NJ, USA). Transmission electron microscopy (TEM) was employed to examine the morphology and structure of CPNs functionalized with holo-Tf. TEM analyses were carried out using a JEM-1400 Flash instrument (JEOL, Tokyo, Japan). CPN dispersions were prepared in Milli-Q water at a concentration of 2.5 mg·L^{-1}, and 50 µL of each sample was deposited onto Formvar-coated copper grids for 5 min prior to imaging. Micrographs were acquired at an accelerating voltage of 120 keV at magnifications corresponding to scale bars of 50, 100, and 500 nm.

https://doi.org/10.2147/IJN.S592688

Following the functionalization process, the amount of holo-Tf bound to or retained by the CPNs was quantified in both filtrate and nanoparticle-retained fractions using the Bicinchoninic Acid (BCA) Protein Assay Kit (Pierce™, Thermo Fisher Scientific). A calibration curve was constructed using serial dilutions of holo-Tf starting from a stock solution of 1 $mg{\cdot}mL^{-1}$, allowing quantification of protein concentrations below 0.01 $mg{\cdot}mL^{-1}$. Absorbance values were recorded at 570 nm and corrected by subtracting the absorbance of reagent blanks (negative controls) measured at the same wavelength. All absorbance measurements were performed using a microplate reader (Multiskan FC, Thermo Fisher Scientific) at 570 nm.

Electrophoretic mobility of CPNs (with and without holo-Tf) was assessed by agarose gel electrophoresis followed by fluorescamine staining for protein detection. A 1% (w/v) agarose gel was prepared in 1× TBE buffer, cast with appropriate combs, and equilibrated in the running tank. Samples, comprising F8BT CPNs covalently functionalized with holo-Tf (EDC/NHS reaction), F8BT CPNs mixed with holo-Tf without EDC/NHS activation, and a holo-Tf positive control, were combined with a freshly prepared fluorescamine solution (1 $mg{\cdot}mL^{-1}$ in DMSO). Each mixture (10 µL) was loaded into individual wells, and electrophoresis was carried out at 80 V for approximately 45 min, or until sufficient band separation was obtained. Following electrophoresis, fluorescent bands were visualized using a gel documentation/fluorescence imaging system under UV (365–395 nm) and blue-light excitation (≈460 nm), equipped with appropriate emission filters (480–520 nm). Representative images were acquired using identical exposure parameters, and fluorescence patterns corresponding to the holo-Tf –fluorescamine conjugate were compared with those of F8BT CPNs using ImageJ (NIH). All procedures involving fluorescamine were performed under low-light conditions, and the reagent was prepared immediately prior to use to ensure consistent derivatization efficiency.

In silico and Cellular Protein-Expression Analysis of TfR1

An in silico survey of transferrin receptor 1 (TfR1/CD71) expression was conducted using the Human Protein Atlas and GEPIA (Gene Expression Profiling Interactive Analysis) based on tumor and normal samples from the TCGA and the GTEx databases (accessed March 2025) to characterize its distribution across tumor types and to compare expression levels in high-grade versus low-grade gliomas and in established GBM cell lines. Based on this bioinformatic analysis, the human GBM cell lines U87MG, T98G and MO59K were selected for experimental validation; HEK-293 (human embryonic kidney) cells were included as non-glioma control.

In addition, representative immunohistochemistry (IHC) images illustrating TfR1 protein expression in human brain tissues were retrieved from the Human Protein Atlas (HPA) database (https://www.proteinatlas.org), an open-access resource providing antibody-based protein expression profiles across normal and cancer tissues. Images corresponding to normal cerebral cortex, low-grade glioma, and GBM samples were examined to qualitatively assess TfR1 protein distribution in human brain tumors. These publicly available data were used to complement the bioinformatic analysis and experimental validation performed in GBM cell lines.

For experimental quantification of TfR1, cells were detached using Accutase, washed twice with ice-cold PBS (1×) and blocked for 15 min on ice in PBS containing 5% FBS. Cells were incubated with purified mouse anti-human CD71 (primary antibody) at a 1:200 dilution for 30 min on ice in the dark. After two washes with PBS, samples were incubated with an Alexa Fluor® 647-conjugated anti-mouse IgG ($F(ab')_2$) secondary antibody at a 1:1000 dilution for 30 min on ice in the dark. Following a final wash, cells were resuspended in PBS for flow cytometric analysis. Appropriate controls (unstained, secondary-only and isotype controls) were processed in parallel.

Flow cytometry was performed on a Guava easyCyte 6–2L instrument (Luminex/Merck Millipore). Data was acquired for a minimum of 10,000 live events per sample after gating on singlets and viable cells and analyzed using FlowJo (v.10). TfR1 expression was reported as the percentage of positive cells and as geometric mean fluorescence intensity (gMFI).

Cellular Uptake of Holo-Tf–Functionalized CPNs and Competition Assay with Free Holo-Tf by Flow Cytometry

We compared the internalization behavior of both F8BT CPNs formulations (functionalized or not with holo-Tf) across GBM and non-tumor cell lines. T98G and U87MG (GBM cells) and HEK-293 (non-tumor cells) cells were seeded in 24-

well plates at 2×10^5 cells·mL^{-1}. After 24 h, cells were incubated with F8BT CPNs or F8BT-Tf CPNs, at an equivalent concentration of 5 mg·L^{-1}. Uptake was evaluated at 0.5, 1, 2 and 4 h post-treatment. Prior to detachment by trypsinization, cells were washed three times with ice-cold PBS to remove non-internalized/extracellular CPNs. Unexposed cells served as negative controls for each cell line.

To assess the contribution of TfR1-mediated uptake, a competition assay was performed using excess free human holo-Tf. Cells were incubated with F8BT-Tf CPNs in the presence of free holo-Tf (1.0 mg·mL^{-1}), and nanoparticle uptake was evaluated 2 h post-incubation. Control conditions included cells exposed to F8BT-Tf CPNs without free holo-Tf, cells treated with non-functionalized F8BT CPNs, and untreated cells.

Fluorescence associated with CPN uptake was quantified by flow cytometry using a Guava easyCyte 6–2L cytometer (Luminex/Merck Millipore). A minimum of 10,000 events were acquired per sample after gating on viable single cells. Data were analyzed using FlowJo software (v10). Uptake was quantified as both the percentage of nanoparticle-positive cells and the gMFI. The inhibitory effect of free holo-Tf was expressed as the reduction in gMFI relative to the corresponding non-blocked condition. Each experiment was performed in two independent biological replicates, with three technical replicates per condition.

Cellular Localization of CPNs Analyzed by Confocal Microscopy

To determine the intracellular localization of CPNs, uptake studies were conducted in GBM cell lines. U87MG and T98G cells were seeded onto round glass coverslips in 24-well plates at a density of 2×10^5 cells·mL^{-1} and incubated with either F8BT CPNs or F8BT-Tf CPNs at a final concentration of 10 mg·L^{-1}. Cells were exposed to the formulations for 30 min or 4 h. After incubation, the medium was removed, and cells were washed three times with PBS to eliminate non-internalized CPNs. Samples were then fixed with 4% paraformaldehyde for 20 min at room temperature. Subsequently, cellular structures were stained using established markers. Nuclei were labeled with Hoechst 33342 (0.5 µM; Sigma-Aldrich) and imaged in the cyan channel (excitation 405 nm, emission 461 nm). F-actin filaments were stained with rhodamine-phalloidin (0.5 µM; Thermo Fisher Scientific) following permeabilization with 0.1% Triton X-100 for 5 min and blocking with 1% BSA for 20 min. Rhodamine-phalloidin was applied for 20 min at room temperature and visualized in the red channel (excitation 559 nm, emission 618 nm). The intrinsic fluorescence of the F8BT CPNs and F8BT-Tf CPNs was detected in the green channel (excitation 488 nm, emission 520 nm). After staining, coverslips were mounted on glass slides using an antifade mounting medium and protected from light prior to imaging. Fluorescence images were acquired using an Olympus FV1200 confocal microscope equipped with appropriate excitation and emission filter sets. Image processing and analysis were performed using Fiji (ImageJ).

In vitro PDT Evaluation of Functionalized-CPNs

To evaluate the photodynamic efficacy of F8BT-PtOEP CPNs in vitro, experiments were performed in U87MG and T98G GBM cell lines. Irradiation was carried out using a multi-LED array (96 LEDs; nominal electrical input 1 W per LED; peak wavelength 460 ± 20 nm). Irradiance at the plate level was measured with a calibrated photodiode power meter (Thorlabs PM100D console with S130C sensor) and found to be 60 mW·cm^{-2}. Cells were seeded in 96-well plates at a density of 2×10^5 cells·mL^{-1} and allowed to adhere for 24 h. Cultures were then exposed to PtOEP-F8BT CPNs, either non-functionalized or conjugated with holo-Tf (F8BT-PtOEP-Tf CPNs), at final concentrations of 1, 2.5, 5 and 10 mg·L^{-1} for an additional 24 h. After nanoparticle incubation, media were removed, and wells were washed two times with PBS to remove non-internalized particles. Cells were irradiated to a nominal fluence of 40 J·cm^{-2}. Based on the measured irradiance, the irradiation duration required to deliver 40 J·cm^{-2} was calculated to be approximately 676.7 s (≈11 min). Dark controls (cells incubated with F8BT-PtOEP CPNs with and without holo-Tf but not exposed to light) and irradiated controls without CPNs were included in every experiment. Cell viability was assessed 24 h after irradiation using the MTT assay. Experiments were performed in three independent series, with $n = 6$ wells per nanoparticle concentration in each series. All conditions were tested with appropriate technical and biological replicates.

Intracellular ROS generated immediately after PDT were quantified using the DCFDA fluorescent probe (Sigma-Aldrich, St. Louis, MO, USA). After nanoparticle incubation (2.5 mg·L^{-1}) and washing, medium was replaced, and cells were irradiated as described above. Immediately after irradiation, cells were loaded with 10 µM DCFDA in serum-free medium for 30 min at 37 °C in the dark. Fluorescence of oxidized DCF (λ_ex = 485 nm; λ_em = 535 nm) was recorded immediately after irradiation by fluorescence microscopy. Control groups included (i) cells treated with CPNs under dark conditions, (ii) cells irradiated without CPNs, and (iii) untreated controls.

To assess PDT-induced morphological damage and loss of membrane integrity, parallel experiments were performed in cells seeded on round coverslips placed in 24-well plates (2×10^5 cells·mL^{-1}). Following nanoparticle incubation and PDT treatment as described above, cells were returned to the incubator for 24 h. Morphological changes were imaged under phase-contrast microscopy (Nikon Eclipse TS100) using constant exposure settings. Membrane integrity was assessed by incubating cells with propidium iodide (PI, Sigma-Aldrich) at a final concentration of 1 µg·mL^{-1} for 20 min at 37 °C in the dark. Red fluorescence (λ_ex = 535 nm; λ_em = 617 nm) was imaged using a fluorescence microscope, and representative fields were recorded. To visualize total nuclei, cells were stained with Hoechst 33342 (Sigma-Aldrich) at a final concentration of 0.5 µM for 10 min at 37 °C. Blue fluorescence was detected using the DAPI/cyan channel (λ_ex = 405 nm, λ_em = 461 nm). Coverslips were rinsed with PBS and mounted with antifade medium. All imaging analyses were performed using Fiji (ImageJ), and at least five random fields were acquired per condition. Control groups were identical to those used for the MTT and ROS assays.

Cell migration was evaluated using a wound healing (scratch) assay. U87MG and T98G cells were seeded in 24-well plates at a density of 2×10^5 cells·mL^{-1} and allowed to reach approximately 90–100% confluence. Cells were then incubated with F8BT-PtOEP CPNs or F8BT-PtOEP-Tf CPNs at a sublethal concentration for 24 h (2.5 mg·L^{-1}). After nanoparticle exposure, PDT was applied under the same irradiation conditions described above.

Immediately after PDT treatment, a linear scratch was generated in the cell monolayer using a sterile pipette tip, and detached cells were removed by washing with PBS. Fresh culture medium was then added, and images of the wound area were acquired at 0 h and 24 h using an inverted microscope.

Wound closure was quantified using ImageJ software by measuring the remaining wound area at each time point and expressed as the percentage of wound closure relative to the initial wound area.

Clonogenic survival after PDT was evaluated using a colony formation assay. U87MG and T98G cells were seeded in 24-well plates at low density and allowed to adhere for 24 h. Cells were then incubated with F8BT-PtOEP CPNs or F8BT-PtOEP-Tf CPNs at concentrations close to the IC_{50} value (10 mg·L^{-1}) for 24 h, followed by PDT under the same irradiation conditions described above. After irradiation, culture medium was replaced with fresh complete medium, and cells were maintained under standard culture conditions for 7 days to allow colony formation. Medium was renewed every 3 days.

At the end of the incubation period, colonies were washed with PBS, fixed with 4% paraformaldehyde for 15 min, and stained with crystal violet solution (1% w/v) for 20 min at room temperature. Excess stain was removed by gentle washing with distilled water, and plates were air-dried prior to imaging. Colonies containing more than 50 cells were considered viable colonies and manually counted under stereoscopic visualization. All experiments were performed in three independent biological replicates.

Biodistribution Analysis of CPNs Using ICP-MS

Biodistribution of F8BT-PtOEP CPNs and F8BT-PtOEP-Tf CPNs was evaluated in NOD/SCID mice bearing orthotopic U87MG-tdiRFP tumors. Tumors were established by stereotactic implantation and allowed to grow for 10 days prior to nanoparticle administration. Mice (n = 4 per group) received a single intravenous dose of 1 mg·kg^{-1} of either F8BT-PtOEP CPNs or F8BT-PtOEP-Tf CPNs. Animals were euthanized 24 h post-injection for organ collection. Because the primary objective of this experiment was to assess nanoparticle deposition at the tumor site and major clearance organs, only liver and brain tissues were harvested for quantitative analysis. Tissues were excised immediately after euthanasia and mechanically homogenized under sterile conditions. Homogenized samples were digested using a microwave-assisted acidic digestion protocol (HNO_3/H_2O_2), ensuring complete dissolution of biological matrices and release of Pt species. Platinum content, corresponding to the PtOEP dopant within the CPNs, was quantified using inductively coupled plasma–mass spectrometry (ICP-MS; PerkinElmer NeXION 1100, Shelton, CT, USA). Three isotopes (^{194}Pt, ^{195}Pt, ^{196}Pt) were monitored to ensure analytical robustness. Calibration curves were generated from certified Pt standards, and matrix-matched fortified blanks and spiked digests were used to assess matrix effects and method recovery, which consistently exceeded 90%. The limit of detection (LOD) for Pt in tissue digests was 1 ppb (μg·kg^{-1}), allowing sensitive quantification of CPN accumulation in the liver and detection of low-level deposition in brain tissue. Samples yielding Pt concentrations below the LOD were reported as "not detected". All results were expressed as μg Pt per kg of wet tissue.

In vivo PDT Evaluation of Functionalized-CPNs in Orthotopic GBM Model

NOD/SCID mice were used for orthotopic GBM xenograft studies. Human GBM cell line stably expressing a near-infrared fluorescent reporter (U87MG-tdiRFP) was used to permit ex vivo NIR tracking of implanted tumors and measurement of volume tumor. For the therapeutic PDT efficacy study, 8-week-old male and female NOD/SCID mice (n = 42) were stereotactically injected in the right cerebral hemisphere with 1×10^5 U87MG-tdiRFP cells. In this cohort, injections were performed under 2% isoflurane anesthesia using a Hamilton micro-syringe and stereotactic coordinates of 2.0 mm lateral and −3.0 mm depth from bregma in a total volume of 3 μL of DMEM (without FBS). Ten days after tumor cells implantation, mice were randomized into six experimental groups (n = 6 per group): (1) Untreated control; (2) Light-only control (cranial irradiation without nanoparticles); (3) F8BT-PtOEP CPNs administered intravenously (i.v.) without irradiation; (4) F8BT-PtOEP CPNs + light, where mice received i.v. nanoparticles followed by irradiation 24 h post-administration; (5) F8BT-PtOEP-Tf CPNs administered i.v. without irradiation; and (6) F8BT-PtOEP-Tf CPNs + light, where mice received i.v. nanoparticles followed by irradiation 24 h post-administration. CPNs were administered as a single intravenous injection (1 mg·kg^{-1}). Illumination was delivered through a minimal cranial trepanation created at the tumor implantation site to allow direct transmission of light into the brain parenchyma while minimizing attenuation by the skull. Irradiation was then performed 24 h after nanoparticle administration using a LED light source coupled to an optical fiber positioned over the cranial opening. Irradiance at the fiber tip was 20 mW·cm^{-2}, and illumination was applied for 10 min, corresponding to a total delivered fluence of 12 J·cm^{-2}.

Animals were monitored daily for neurological signs and general condition. Overall survival was recorded as the primary efficacy endpoint. Mice were humanely euthanized upon presentation of severe neurological deficits or marked deterioration in general conditions. At the time of euthanasia, brains were carefully excised and immediately processed for both ex vivo fluorescence imaging and histopathological analysis. Ex vivo near-infrared imaging was performed using an Odyssey imaging system to confirm tumor presence and quantify tumor burden based on tdiRFP fluorescence.

For histopathological analysis, whole brains, including the tumor-bearing hemisphere, were immersion-fixed in 4% buffered paraformaldehyde for 24–48 h at 4 °C. Fixed tissues were dehydrated through a graded ethanol series, cleared in xylene, and paraffin-embedded using standard histology protocols. Coronal sections (5 μm) were cut using a rotary microtome to consistently capture the tumor epicenter and surrounding parenchyma. Sections were mounted on glass slides, deparaffinized in xylene, and rehydrated through descending ethanol concentrations following Hematoxylin and eosin (H&E) staining. Histological assessment focused on tumor cellularity, infiltrative patterns, vascular changes (angiogenesis, tortuosity, endothelial hyperplasia), necrosis, hemorrhage, mitotic activity, and cytopathic features such as apoptosis and pyknosis.

Brightfield micrographs were acquired using a Carl Zeiss binocular microscope with LED illumination coupled to an AmScope 20-MP CMOS C-mount microscope camera. Digital images were captured under identical exposure and magnification settings. Microphotographs were visualized and annotated using NDP.view2 (Hamamatsu Photonics) software. Representative low- and high-magnification fields were selected for qualitative and semi-quantitative histopathological evaluation.

All procedures were conducted in accordance with institutional animal care and use guidelines and approved protocols; analgesia and predefined humane endpoints were used throughout to minimize animal suffering.

Statistical Analysis

All quantitative data are presented as mean ± standard deviation (SD) unless otherwise stated. The number of biological replicates (n) and technical replicates are reported in the figure legends and Results; in brief, in vitro experiments represent at least three independent biological experiments with the indicated number of technical replicates per experiment, and in vivo cohorts comprised n = 6 animals per group unless noted.

Prior to hypothesis testing, data were inspected for normality (Shapiro–Wilk test) and homogeneity of variance (Levene's test). For comparisons involving three or more groups, one-way ANOVA (or two-way ANOVA for factors with two independent variables or time-course data) was employed for normally distributed data, followed by Tukey's multiple-comparisons post hoc test. Dose–response curves were fitted by nonlinear regression and half-maximal inhibitory concentrations (IC_{50}) were compared by extra-sum-of-squares F-test. Correlations were assessed by Pearson's r for parametric data or Spearman's ρ for nonparametric data.

Survival data were analyzed by the Kaplan–Meier method and group comparisons were made using the log-rank (Mantel–Cox) test. Hazard ratios and 95% confidence intervals were estimated with a Cox proportional-hazards model when appropriate. Animals reaching predefined humane endpoints were censored according to the protocol.

All statistical tests were two-tailed. A threshold of $p < 0.05$ was considered statistically significant; exact p-values are reported in the text or figure legends, except where $p < 0.001$ is indicated. Statistical analyses and figure preparation were performed using GraphPad Prism (v.9; GraphPad Software, San Diego, CA, USA).

Results

Design, Synthesis and Holo-Tf Functionalization of CPNs

CPNs were prepared by the controlled nanoprecipitation method as previously described.[8] Polymer chains that were initially extended in the good solvent (THF) undergo rapid collapse upon mixing with the poor solvent (water), yielding small, spherical nanoaggregates. PSMA was co-precipitated with the CP to yield stabilized CPNs, introducing surface carboxylate groups through hydrolysis of the maleic anhydride units contained in the PSMA in aqueous medium.[23] These anionic surface groups not only enhance colloidal stability but also provide convenient chemical moieties for subsequent covalent bioconjugation.

To generate actively targeted nanoparticles, CPNs were covalently functionalized with holo-Tf to enable interaction with TfR1 overexpressed at the BBB and on GBM cells.[24] Surface carboxylates were activated for amide bond formation using the EDC/NHS coupling strategy. Primary amines available for conjugation are located at the N-terminal alpha-amine of each polypeptide chain and in the ε-amine group of lysine side chains; because these amine groups are typically solvent-exposed, they are readily accessible for conjugation without substantially perturbing the protein fold.[25] Holo-Tf contains 19 lysine residues distributed throughout its structure, providing multiple potential sites for covalent attachment. Following surface conjugation, F8BT-based CPNs were characterized and compared to unbound CPNs.

F8BT CPNs exhibited a number-average d_h of 22 ± 5 nm with a PDI of 0.3 ± 0.1, whereas F8BT-PtOEP CPNs showed a d_h of 21 ± 3 nm with a PDI of 0.4 ± 0.1 (Figure 2A). Following covalent conjugation with holo-Tf, the d_h increased to 54 ± 3 nm (PDI 0.3 ± 0.1) for F8BT-Tf CPNs and to 42 ± 8 nm (PDI 0.2 ± 0.1) for F8BT-PtOEP-Tf CPNs, consistent with formation of a covalently bound protein corona around nanoparticles. Concomitant changes in surface charge were observed after protein coupling. F8BT CPNs displayed an initial ζ of −42.1 ± 0.2 mV that shifted to −35.8 ± 0.8 mV after holo-Tf conjugation. Similarly, F8BT-PtOEP CPNs changed from −41.4 ± 0.3 mV to −36 ± 1 mV upon functionalization with holo-Tf (Figure 2B). The reduction in the magnitude of the negative ζ indicates a decrease in surface negative charge density upon protein attachment. Holo-Tf has a reported ζ of approximately −8 mV in water at neutral pH and presents surface regions of positive charge, which can partially neutralize the carboxylate anions of the PSMA corona.[26] Taken together, the increase in d_h and the shift toward less negative zeta potentials provide complementary evidence of successful holo-Tf conjugation, while the observed PDIs indicate that colloidal dispersity remained within acceptable limits after functionalization.

TEM micrographs of F8BT CPNs and F8BT-PtOEP CPNs are shown in Figure 2C. In the undecorated preparation, CPNs appear as numerous well-dispersed, roughly spherical dry-state cores with diameters in the order of ~15–30 nm (shown in the high-magnification insets). In the holo-Tf-decorated sample, individual polymer cores of similar size are still evident in the high-magnification insets; however, the particles display an increased tendency to form small, loose aggregates upon deposition and exhibit a subtle, lower-contrast halo surrounding cores in several regions. This peripheral contrast is compatible with a covalently linked protein layer (protein corona) resulting from holo-Tf functionalization.

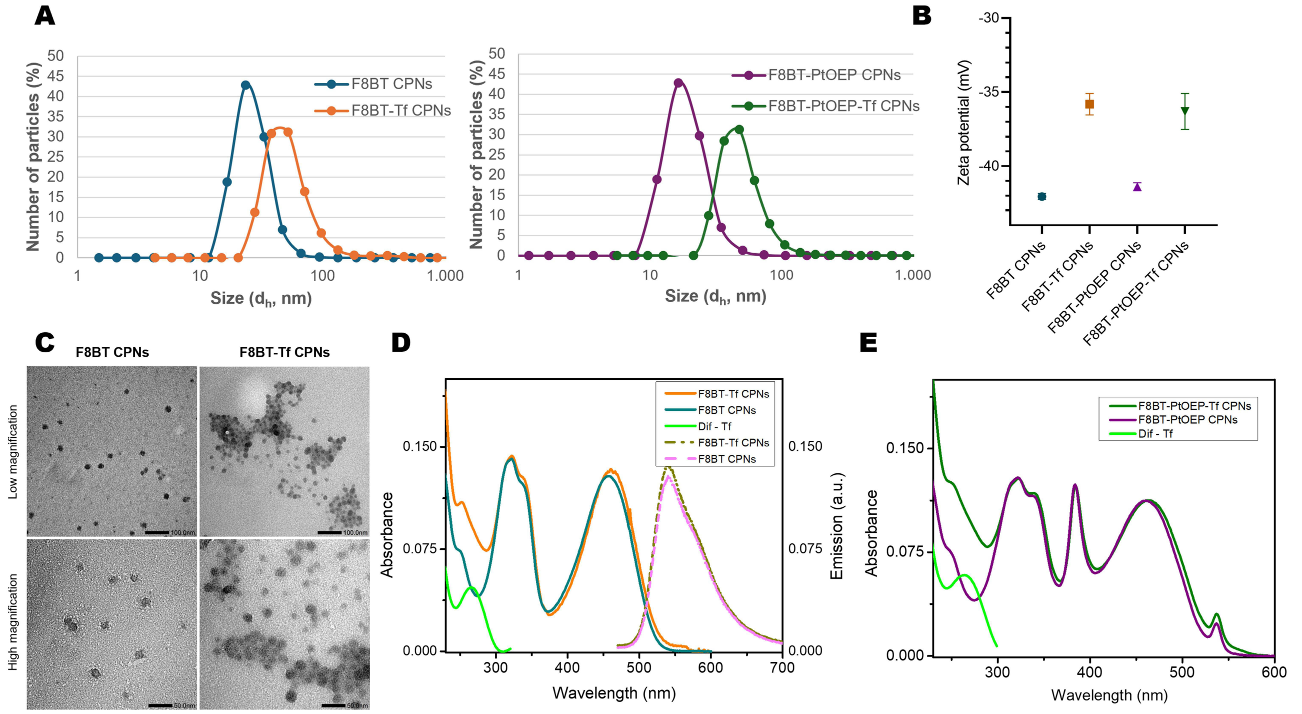

Figure 2 Physicochemical characterization of F8BT-based CPNs before and after holo-Tf functionalization. (**A**) Size distribution (average hydrodynamic diameter (d_h nm) of functionalized F8BT CPNs and F8BT-PtOEP CPNs dispersions. (**B**) Zeta potential values of CPNs before and after holo-Tf conjugation. The surface charge became less negative upon functionalization, consistent with protein adsorption on the nanoparticle surface. (**C**) Transmission electron microscopy (TEM) images of non-functionalized F8BT CPNs and holo-Tf functionalized F8BT-Tf CPNs. Upper panels show lower-magnification images illustrating nanoparticle dispersion on the TEM grid, while lower panels show higher-magnification images highlighting particle morphology. Both nanoparticle formulations exhibit quasi-spherical morphology with sizes below ~50 nm. Occasional small clusters observed in the images likely arise from drying effects during TEM grid preparation. (**D**) Absorption (normalized at 320 nm) and emission spectra of F8BT CPNs, (**E**) Absorption spectra of F8BT-PtOEP CPNs showing the characteristic F8BT absorption band at 460 nm and the PtOEP Soret and Q bands at 384 and 537 nm, respectively. The shoulder near 264 nm in holo-Tf–functionalized samples indicates the presence of the protein. Overall, these data confirm successful conjugation of holo-Tf (λmax ~280 nm,[27]) to the nanoparticle surface without altering the optical properties of the CP core.

Bioconjugation Efficiency and Photophysical Properties

Figure 2D and E present the UV–visible absorption spectra (normalized at 320 nm) of F8BT CPNs and F8BT-PtOEP CPNs, each shown before and after holo-Tf functionalization. The prominent absorption band centered at 460 nm is attributable to the F8BT polymer.[8] In F8BT-PtOEP CPNs (Figure 2E), additional transitions corresponding to the PtOEP Soret and Q bands are observed at ~384 nm and ~537 nm, respectively. The absorption profiles of protein-functionalized and non-functionalized CPNs are largely superimposed, with the notable exception of an extra shoulder appearing below 300 nm in the holo-Tf-decorated samples. The differential spectrum (green line) highlights an additional absorption feature centered at ~264 nm, associated with the presence of holo-Tf bound to the CPNs.[28] This band is shifted relative to the characteristic holo-Tf maximum at ~284 nm in water,[27] consistent with a hypsochromic (blue) shift induced by its interaction with the hydrophobic CPN surface.

Using the absorbances measured at 264 nm (A = 0.046 for undoped CPNs and A = 0.058 for PtOEP-doped CPNs), together with a molar extinction coefficient (ε) of ~83,400 $M^{-1}\cdot cm^{-1}$ for holo-Tf[26] and a molecular weight of 75,200 $g\cdot mol^{-1}$, the holo-Tf concentrations associated with the CPNs are estimated to be ~0.042 $mg\cdot mL^{-1}$ (undoped) and ~0.052 $mg\cdot mL^{-1}$ (PtOEP-doped), respectively. Given an initial holo-Tf input of 0.054 $mg\cdot mL^{-1}$ during functionalization, these values indicate that a substantial fraction of the protein remains associated with the CPNs (~78% for the undoped and ~97% for the PtOEP-doped formulations). These estimates should be considered approximate, as they rely on the extinction coefficient measured at 284 nm and do not account for potential changes in ε arising from the hypsochromic shift or matrix effects; nevertheless, they support that an important fraction of holo-Tf remains bound to the nanoparticle surface.

Furthermore, to quantify the proportion of holo-Tf covalently attached to the nanoparticle surface, protein concentrations were assessed in three sample fractions: the aqueous solution obtained post-filtration (filtrate), the nanoparticle-containing fraction after centrifugation and resuspension, and control samples of non-bioconjugated CPNs to evaluate background signal. A calibration curve was established using progressive dilutions of holo-Tf, starting at 1 $mg{\cdot}mL^{-1}$, employing the BCA kit (Figure S1). The protein masses in the nanoparticle and filtrate fractions were determined using the absorbances and the calibration curve, while the percentage of holo-Tf bound to the CPNs was estimated as the ratio of total recovered protein linked to the nanoparticle sample. Employing this methodology, PtOEP-F8BT-Tf CPNs preserved around ~84% of the input holo-Tf (with roughly ~16% recovered in the filter), whereas F8BT-Tf CPNs kept about ~79% of the holo-Tf (with approximately ~21% recovered in the filtrate). The non-conjugated CPN controls produced minimal signal above the background, so validating the specificity of the test. The results demonstrate effective functionalization, with over 75% of the applied holo-Tf retained on the CPNs post-purification.

To provide additional evidence for protein binding to the CPNs, an electrophoretic mobility assay of the F8BT-PSMA CPNs was conducted on a 1% agarose gel, allowing observation of mobility changes arising from variations in size and/or zeta potential between protein-functionalized and non-functionalized CPNs, and enabling assessment of holo-Tf binding. As shown in Figure S2, holo-Tf–functionalized CPNs prepared with EDC/NHS displayed reduced mobility relative to their non-functionalized counterparts. This behavior is consistent with the increase in size and the decrease in zeta potential observed for functionalized CPNs. In addition, fluorescamine protein staining together with the electrophoretic mobility assay confirmed that holo-Tf is covalently attached to the CPN surface.

To complete the photophysical characterization of the F8BT-based CPNs, their fluorescence properties were evaluated. These measurements were performed only for F8BT CPNs and F8BT-Tf CPNs, as PtOEP-doped formulations exhibit very low fluorescence quantum yields ($\Phi f < 0.1\%$).[10] As shown in Figure 2D, the emission spectra recorded upon excitation at 460 nm are essentially identical for functionalized and non-functionalized F8BT CPNs, indicating that holo-Tf conjugation does not perturb the F8BT fluorophores. Importantly, both emission spectra were acquired from nanoparticle dispersions adjusted to the same absorbance (<0.1) at the excitation wavelength (456 nm) to minimize inner-filter effects and ensure direct comparability.

TfR1 Expression in Gliomas and Selection of Cellular Models

TfR1 is found in cells from several organs, particularly those characterized by a rapid rate of cell division, including blood cells, enterocytes, and monocytes. Moreover, it is present in endothelial cells constituting the BBB and in brain tissue, including both neuronal and glial cells.[29] An integrated in silico and experimental analysis of transferrin receptor 1 (TfR1/TFRC) expression was performed to define suitable cellular models for transferrin-targeted nanoparticle studies. A database search was performed to examine TfR1 expression across different tissues and cell lines. Data from The Human Protein Atlas and GEPIA were analyzed to gather pertinent information on TfR1 gene expression across various GBM subtypes and distinct GBM cell lines (Figure 3A–C). Specifically, the data indicated that TFRC transcript levels are elevated in high-grade gliomas compared with low-grade gliomas, and that expression varies across canonical molecular subtypes (Figure 3A and B). Pairwise comparisons in the dataset revealed statistically significant differences between selected groups (brackets and asterisks in the plots), supporting the relevance of TfR1 as a GBM-associated target. Moreover, analysis of mRNA expression data from the Human Protein Atlas indicates that the U87MG cell line (derived from GBM) exhibits elevated TFRC/TfR1 expression, whereas HEK293 cells (of human embryonic kidney origin) display minimal receptor expression (Figure 3C). These bioinformatic findings were experimentally validated by flow cytometry in GBM and non-tumoral cell lines (U87MG, T98G, MO59K and HEK293). Representative histograms (Figure 3D) show minimal signal in unstained and secondary antibody-only controls (red and orange traces) and a pronounced rightward shift following specific anti-CD71 staining (blue trace) in the GBM cell lines. Quantitative analysis demonstrates that U87MG and MO59K display the highest proportion of TfR1-positive cells (Figure 3F) and the greatest gMFI (Figure 3E), consistent with robust surface expression. T98G exhibited intermediate/lower staining, whereas HEK293 cells showed only low-level TfR1 detection, confirming their utility as a non-tumor control.

The in silico and flow cytometric results collectively indicate that TfR1 is increased in GBM and is significantly expressed in U87MG and MO59K cells compared to the non-tumor HEK293 control. These findings confirm the

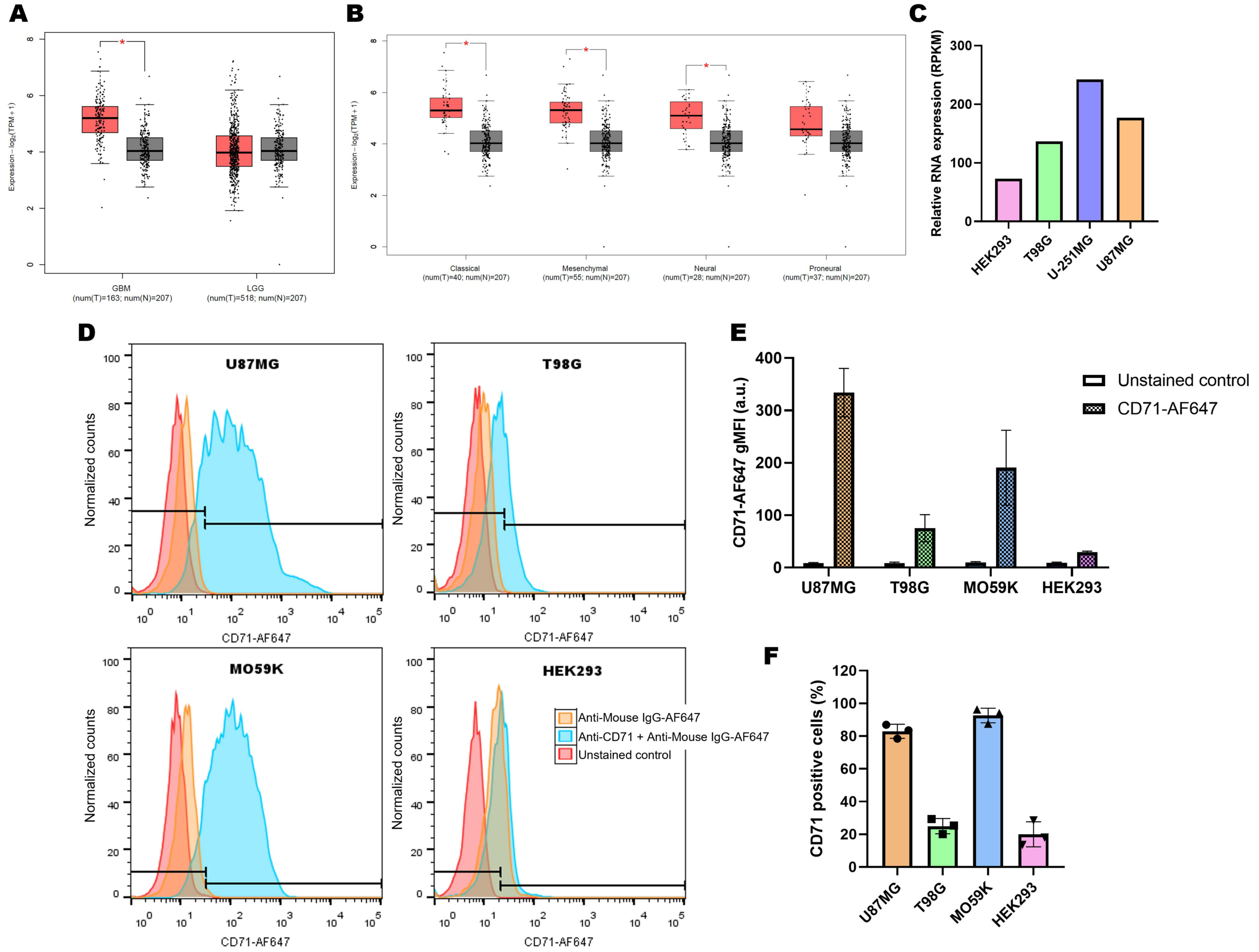

Figure 3 Integrated in silico and experimental analysis of transferrin receptor 1 (TfR1 / TFRC) expression in gliomas and representative cell lines. Box-plot summary of TFRC mRNA expression obtained from GEPIA (Gene Expression Profiling Interactive Analysis) based on tumor and normal samples from the TCGA and the GTEx databases (accessed March 2025). (**A**) Comparison of TFRC expression in high-grade gliomas (GBM) vs. low-grade glioma (LGG) (n indicated on each plot). (**B**) TFRC expression stratified by canonical GBM molecular subtype (classical, mesenchymal, neural, proneural). Boxes represent the interquartile range, horizontal lines the median, whiskers extend to 1.5×IQR, and individual data points are overlaid. Brackets with asterisks denote statistically significant pairwise differences (see Methods for statistical test). (**C**) TfR1 expression levels in GBM cell lines and HEK293 (non-tumor control). Data taken and adapted from the Human Protein Atlas. (**D**) Representative flow-cytometry histograms of surface TfR1 staining in U87MG, T98G, MO59K and HEK293 cells. Traces correspond to unstained control (red), secondary-only control (anti-mouse IgG–AF647; Orange) and specific anti-CD71 primary staining followed by anti-mouse-AF647 secondary (blue). The horizontal bracket on each histogram indicates the gate used to define TfR1-positive events. (**E**) gMFI of the CD71 signal (mean ± SD; n = biological replicates indicated in Methods), and (**F**) percentage of TfR1-positive cells. Data were normalized to appropriate controls. Statistical comparisons were performed as described in Methods (*$p < 0.05$).

selection of U87MG and T98G as TfR-high and TfR-low models for further nanoparticle uptake and photodynamic effectiveness studies, so reinforcing the translational justification for utilizing TfR1 as a pathway for targeted delivery to GBM.

Representative immunohistochemistry images retrieved from the Human Protein Atlas further illustrate the differential expression of TfR1 in human brain tissues, showing low staining in normal cerebral cortex and increased expression in glioma samples, particularly in GBM (Figure S3).

Cell Uptake and Binding Evaluation of CPNs Functionalized with Tf

Cellular uptake of F8BT CPNs in tumor cell lines was evaluated using flow cytometry. All nanoparticle incubations were performed in complete culture medium containing 10% FBS to mimic physiological protein exposure; although serum proteins can promote formation of a biomolecular corona and potentially mask targeting ligands, this condition better reflects the in vivo milieu. Under these serum-containing conditions, F8BT CPNs functionalized with holo-Tf exhibited significantly higher uptake in the U87MG cell line at all time points tested. After 1 h of exposure, 42% of the cells treated with F8BT-Tf CPNs showed significant uptake, compared to 18% observed with F8BT CPNs. At 2 h, these values were 48% and 19%, respectively (Figure 4A). In the T98G cell line, characterized by low TfR1 expression, the trend remained; F8BT-Tf CPNs reached uptake levels of 4% at 1 hour and 7% at 2 hours (Figure 4B). Holo-Tf functionalization improved cellular uptake in both GBM cell lines, with a notable effect in the cell line expressing the highest level of TfR1 (U87MG). Additionally, the uptake of F8BT CPNs with and without holo-Tf was analyzed by comparing the gMFI per cell at 0.5, 1, and 4 h. In U87MG cells, the uptake of F8BT-Tf CPNs was significantly higher than that of F8BT CPNs, with a time-dependent increase (Figure 4C). At 4 h, the F8BT-Tf CPNs reached an gMFI value of 211, while the F8BT CPNs showed a value of 73. Statistically significant differences were observed between the two F8BT CPNs at 0.5, 1, and 4 h ($p = 0.0113$, $p = 0.0095$, and $p < 0.0001$, respectively). A similar behavior was observed in T98G, where F8BT-Tf CPNs exhibited an gMFI of 150 at 4 h, compared to 43 for F8BT CPNs. However, at the 0.5- and 1-hour time points, no significant differences were detected between the two types of F8BT CPNs ($p = 0.9404$ and $p = 0.3486$) (Figure 4D). At 2 h post-incubation, quantitative analysis by flow cytometry revealed that holo-Tf functionalization substantially enhanced nanoparticle uptake in both GBM cell lines relative to non-functionalized F8BT CPNs (Figure 4E). Cells exposed to F8BT-Tf CPNs showed markedly higher fluorescence intensity and a larger fraction of nanoparticle-positive events than cells treated with non-functionalized F8BT CPNs or untreated controls. Importantly, the presence of excess free holo-Tf (1.0 mg·mL^{-1}) produced a pronounced reduction in the uptake of F8BT-Tf CPNs, decreasing the fluorescence signal to levels comparable to those observed for non-functionalized particles. This competitive inhibition is consistent with TfR-dependent internalization of holo-Tf–functionalized CPNs. Notably, a measurable residual uptake remained after competition, indicating that additional TfR-independent pathways may also contribute to CPN internalization. These findings support a predominant role for receptor-mediated endocytosis in the enhanced cellular accumulation of holo-Tf-decorated CPNs while acknowledging the contribution of mixed uptake mechanisms.

To complement the quantitative flow cytometry analysis, confocal microscopy was used to qualitatively visualize the intracellular distribution of the nanoparticles. In this context, cytoskeletal staining was employed to provide morphological reference for the localization of internalized CPNs rather than to assess membrane binding. Confocal imaging of U87MG and T98G monolayers after 30 min exposure to F8BT CPNs (with and without holo-Tf) revealed a punctate, nanoparticle-associated fluorescence pattern in cell membrane and cytoplasm (Figure 4F). In untreated controls only background fluorescence was observed. Cells treated with non-functionalized F8BT CPNs exhibited discrete green puncta predominantly at or immediately below the cell membrane, frequently aligned with the basal optical plane (dashed line), whereas F8BT-Tf CPNs produced a noticeably greater number of punctate structures that were more widely distributed throughout the cytoplasm. Orthogonal (xz/yz) projections confirm that nanoparticle signal for both formulations extends beneath the plasma membrane into the cell interior, consistent with internalization rather than mere surface adsorption. F-actin staining (rhodamine-phalloidin, red) demonstrates intact cytoskeletal architecture after nanoparticle exposure, and Hoechst (blue) marks nuclei; no gross morphological disruption was evident at this early time point. The increased abundance and deeper cytoplasmic distribution of green puncta following F8BT-Tf CPNs are suggestive of enhanced, likely receptor-mediated uptake of the Tf-decorated CPNs.

In vitro Photodynamic Performance of F8BT-PtOEP-Tf CPNs

To investigate the photodynamic activity of Tf-functionalized CPNs, U87MG and T98G GBM cell lines were incubated for 24 h with increasing concentrations (1–10 mg·L^{-1}) of F8BT-PtOEP CPNs and F8BT-PtOEP-Tf CPNs prior to irradiation (40 J·cm^{-2}). Cell viability, assessed by MTT assay 24 h post-PDT, revealed a concentration-dependent reduction in viability for both formulations (Figure 5A and B). U87MG cells, which express higher levels of TfR1, exhibited significantly greater sensitivity to F8BT-PtOEP-Tf CPNs, with viability decreasing to 32 ± 4% at 10 mg·L^{-1} compared to 48 ± 6% for non-functionalized CPNs (Figure 5A) ($p < 0.001$). Similar trends were observed in T98G cells, although the magnitude of the effect was lower, consistent with their reduced TfR1 expression. In the T98G cell line, treatment with F8BT-PtOEP CPNs under irradiation resulted in an IC_{50} of 9.5 mg·L^{-1}. With the addition of F8BT-PtOEP -Tf CPNs, the IC_{50} decreased slightly to 9 mg·L^{-1}, suggesting that the presence of holo-Tf could reduce the dose required

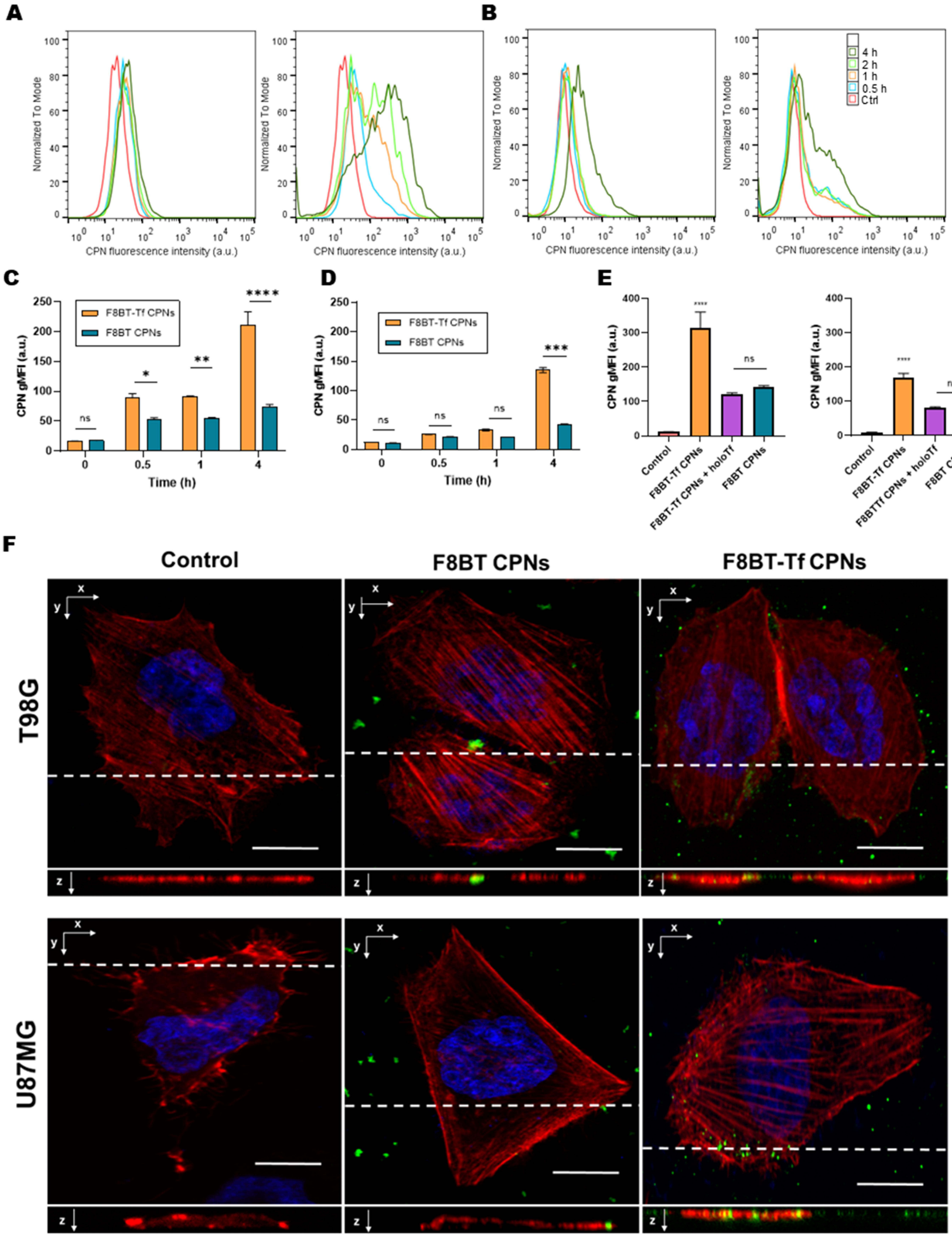

Figure 4 Time-course and competition analysis of cellular uptake of F8BT CPNs with and without holo-Tf. (**A** and **B**) Representative flow-cytometry histograms showing nanoparticle-associated fluorescence in U87MG and T98G cells at the indicated incubation times (0.5, 1, 2 and 4 h). Unexposed control cells (Ctrl) are shown in red; histograms corresponding to successive time points are overlaid to illustrate the progressive accumulation of nanoparticle signal. (**C** and **D**) Quantification of uptake kinetics derived from flow-cytometry data, expressed as geometric mean fluorescence intensity (gMFI) as a function of incubation time for non-functionalized F8BT CPNs and holo-Tf-functionalized F8BT-Tf CPNs. Error bars represent SD. (**E**) Competition assay performed 2 h post-incubation showing that the presence of excess free holo-Tf significantly reduces the uptake of F8BT-Tf CPNs relative to non-competed F8BT-Tf CPNs, whereas uptake of non-functionalized F8BT CPNs is minimally affected. (**F**) Representative confocal micrographs showing intracellular localization of CPNs (green), F-actin (rhodamine-phalloidin, red), and nuclei (Hoechst, blue) after 30 min exposure. Orthogonal (xz) projections confirm intracellular, sub-membrane localization of the punctate nanoparticle signal; dashed lines indicate the focal plane used for orthogonal projections. Scale bars = 20 μm. Statistical significance: ns, not significant; *$p < 0.05$; **$p < 0.01$; ***$p < 0.001$; ****$p < 0.0001$.

https://doi.org/10.2147/IJN.S592688

to achieve 50% cell inhibition. However, this difference was not statistically significant (*$p = 0.84$*) (Figure 5B). In the U87MG cell line, previously reported to exhibit higher TfR1 expression, an IC_{50} of 9.9 $mg\cdot L^{-1}$ was observed after irradiation with F8BT-PtOEP-Tf CPNs. In contrast, when the cells were irradiated with F8BT-PtOEP CPNs, the IC_{50} was 19.3 $mg\cdot L^{-1}$. Unlike what was observed in the T98G cell line, the use of holo-Tf in this case halved the dose required to reach the IC_{50} (*$p = 0.0006$*), which could be attributed to TfR1 overexpression.

Immediately after PDT, ROS generation was evaluated using the DCFDA fluorescence assay (Figure 5C). Bright green fluorescence corresponding to oxidized DCF confirmed the production of intracellular ROS following light activation. The fluorescence intensity was markedly higher in cells treated with F8BT-PtOEP-Tf CPNs than in those

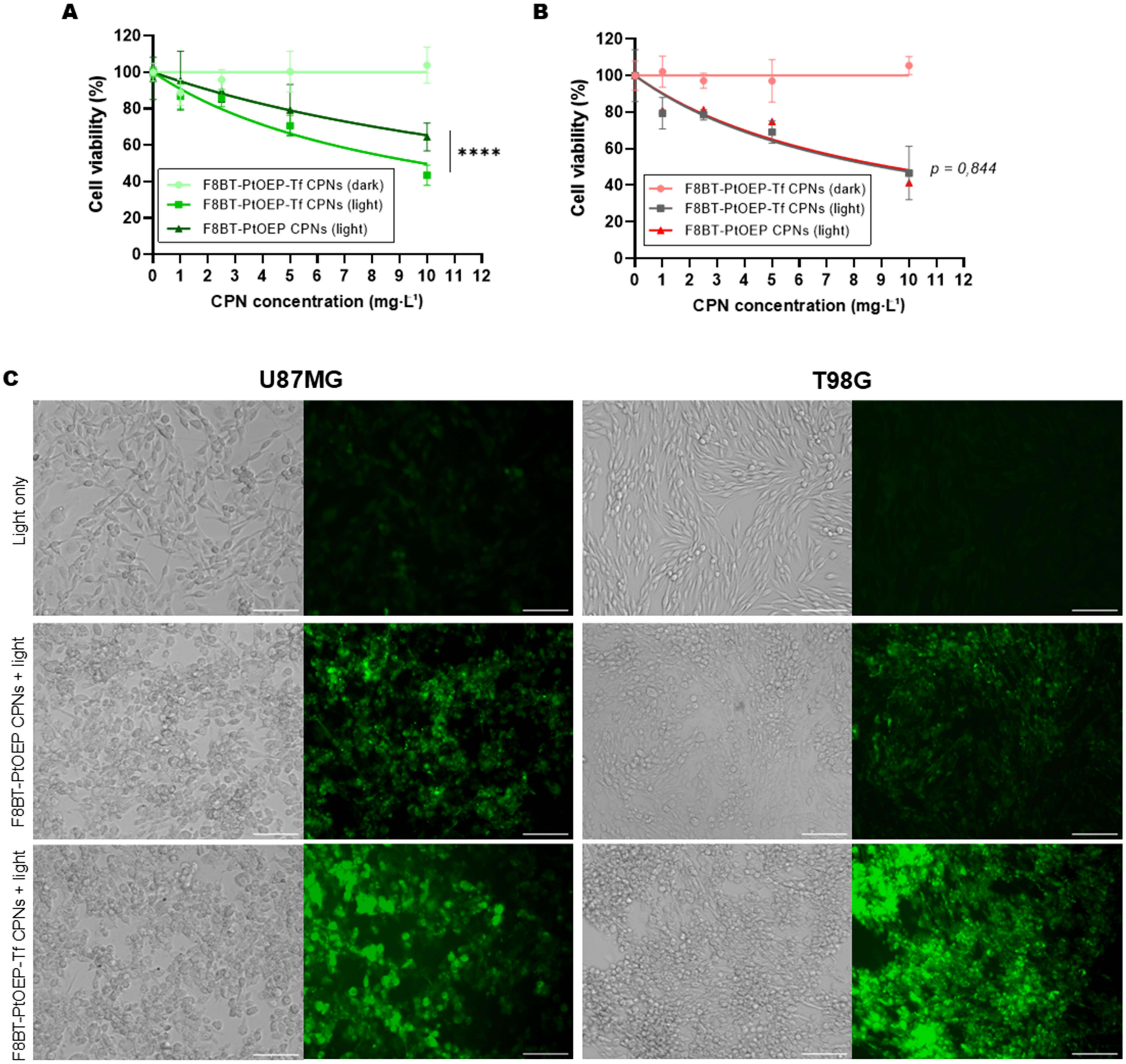

Figure 5 Photodynamic cytotoxicity of F8BT-PtOEP CPNs with and without holo-Tf in GBM cell lines. (**A**) Cell viability of U87MG and (**B**) T98G cells after 24 h incubation with increasing concentrations (1–10 $mg\cdot L^{-1}$) of F8BT-PtOEP CPNs or F8BT-PtOEP-Tf CPNs, followed by blue light irradiation (40 $J\cdot cm^{-2}$). Cell viability was determined 24 h post-irradiation using the MTT assay. Data are expressed as mean ± SD (n = 6). Curves represent independent nonlinear regression fits generated in GraphPad Prism for each treatment group. Asterisks indicate statistically significant differences between treatments (two-way ANOVA, ****$p < 0.0001$). (**C**) Representative phase-contrast and fluorescence microscopy images (20×) showing intracellular ROS production immediately after PDT, as measured by DCFDA staining (green fluorescence). In both U87MG and T98G cells, increased green fluorescence intensity correlates with holo-Tf functionalization and increased CPNs internalization, indicating enhanced ROS generation. Control (light only) samples show negligible fluorescence, confirming CPNs and light-dependent activation. Scale bar = 100 μm.

treated with non-functionalized CPNs, indicating enhanced photoactivation and oxidative stress. This effect was most pronounced in U87MG cells, correlating with the increased nanoparticle uptake observed in previous assays. Control samples maintained in the dark displayed negligible fluorescence, confirming that ROS formation was strictly dependent on photoexcitation of CPNs. These data demonstrate that holo-Tf functionalization not only promotes receptor-mediated internalization of F8BT-PtOEP-Tf CPNs but also amplifies PDT-induced ROS generation and subsequent cytotoxicity in TfR-overexpressing GBM cells.

Morphological assessment and PI staining further supported the cytotoxic effects observed in the MTT and ROS assays. Phase-contrast imaging performed 24 h after PDT revealed profound alterations in U87MG and T98G cell morphology following treatment with F8BT-PtOEP-Tf CPNs, including cell rounding, detachment, and loss of monolayer integrity, consistent with extensive photodamage (Figures S4 and S5). Correspondingly, PI staining showed a marked increase in red-fluorescent nuclei in irradiated cultures, indicating compromised membrane integrity and cell death. In both cell lines, the extent of PI-positive cells was greater in the holo-Tf groups than in those exposed to non-functionalized CPNs, mirroring the differences observed in ROS production and viability assays. Control groups maintained in the dark exhibited largely intact morphology and minimal PI uptake, confirming that cytotoxicity arose specifically from light-activated photodynamic mechanisms.

To further investigate whether nanoparticle-mediated PDT affects GBM cell migration, a wound healing assay was performed using a sublethal nanoparticle concentration (2.5 mg·L^{-1}). As shown in Figure S6, cells treated with F8BT-PtOEP-Tf CPNs followed by light irradiation exhibited a marked reduction in wound closure compared with control conditions. In contrast, treatment with nanoparticles alone or light alone produced only modest effects on cell migration. These results suggest that PDT mediated by holoTf-functionalized CPNs significantly impairs the migratory capacity of GBM cells.

To further assess the long-term antiproliferative effects of PDT, clonogenic survival assays were performed in U87MG and T98G cells using nanoparticle concentrations close to the IC_{50} value (10 mg·L^{-1}). As shown in Figure S7, PDT mediated by both nanoparticle formulations reduced colony formation compared with irradiated controls; however, the effect was more pronounced in cells treated with F8BT-PtOEP-Tf CPNs + light. In U87MG cells, holo-Tf-functionalized CPNs markedly impaired clonogenic survival, resulting in a substantial reduction in the number and size of colonies relative to non-functionalized nanoparticles. In contrast, T98G cells showed a more moderate decrease in colony formation, consistent with their lower TfR1 expression and reduced sensitivity to Tf-targeted PDT observed in the viability assays. These findings indicate that holo-Tf functionalization enhances the ability of F8BT-PtOEP CPNs-mediated PDT not only to induce acute cytotoxicity, but also to compromise the long-term reproductive capacity of GBM cells.

Orthotopic GBM Model, Biodistribution and in vivo Therapeutic Efficacy of F8BT-PtOEP-Tf CPNs

To advance the study of the therapeutic efficacy of F8BT-PtOEP-Tf CPNs in PDT protocols, it is essential to develop robust orthotopic preclinical models. In this regard, an assay was designed to induce GBM tumors in immunocompromised NOD/SCID mice using U87MG-tdiRFP cells to evaluate growth kinetics and the onset of neurological signs associated with the disease. These cells were modified to express a near-infrared fluorescent protein, which facilitates in vivo and ex vivo tracking.

Tumor development was monitored clinically every 24 h, assessing changes in behavior and the onset of signs such as anorexia, depression, lethargy, ataxia, and seizures. A minimum of 10 days elapsed after cell injection before neurological signs appeared. This time was later defined as the start of nanoparticle treatment and the application of PDT. A tumor formation rate of 100% was recorded in mice implanted with U87MG-tdiRFP. Starting from day 10 post-implantation, the mice exhibited initial signs including dorsal curvature, lethargy, reduced grooming behavior, and partial seizures. From days 15 to 20, the subjects exhibited progression to generalized seizures, depression, and anorexia, leading to the termination of the experiment. The mice underwent euthanasia via cardiac perfusion while under general anesthesia. NIR fluorescence emission confirmed the presence of tumors, enabling accurate visualization of their location and extent (Figure S8).

Tumor growth was analyzed histopathologically, demonstrating an infiltrative pattern that displaces and disrupts normal brain architecture. All samples exhibited poorly defined regions of laminar hemorrhage and significant cellular pleomorphism. Marked anisokaryosis and anisocytosis were observed, accompanied by a high mitotic rate of 6 to 8 mitotic figures per 2.37 cm^2 of tissue, indicating the tumor's significant proliferative potential. Furthermore, glomerular capillary tufts containing numerous erythrocytes were noted, indicating a significant nutritional requirement of the tumor (Figure S8).

To validate the therapeutic potential of F8BT-PtOEP-Tf CPNs formulations under clinically relevant conditions, we established an orthotopic PDT treatment workflow as schematized in Figure 6A. Briefly, U87MG-tdiRFP cells were implanted stereotactically into the right striatum (day 0), and tumors were allowed to progress for ten days, at which point neurological signs and NIR emission confirmed successful engraftment. On day 10, mice received an intravenous injection of either F8BT-PtOEP CPNs or F8BT-PtOEP-Tf CPNs, and 24 h later (day 11), a fiber-optic LED illumination protocol was applied following a minimal cranial trepanation to ensure adequate intraparenchymal light delivery. Thereafter, animals were monitored for survival as the primary therapeutic endpoint. This experimental timeline enabled synchronized nanoparticle administration, localized brain irradiation, and longitudinal assessment of treatment efficacy in a robust orthotopic GBM model.

Biodistribution was evaluated 24 h after i.v. administration of F8BT-PtOEP CPNs and F8BT-PtOEP-Tf CPNs using ICP-MS, taking advantage of the PtOEP dopant as an elemental tracer as previously we reported.[15] The analytical method exhibited a limit of detection (LOD) of 1 ppb for Pt, permitting sensitive quantification of nanoparticle deposition in tissues (n = 4). As shown in Figure 6B, both CPN formulations displayed a predominant accumulation in the liver, consistent with expected hepatobiliary clearance of polymeric nanomaterials.

Importantly, quantification in brain tissue revealed a detectable Pt signal exclusively in animals treated with F8BT-PtOEP-Tf CPNs, whereas Pt levels in brains from the F8BT-PtOEP CPNs group remained below the LOD. These data indicate that holo-Tf functionalization enables measurable nanoparticle accumulation within the brain parenchyma, likely reflecting TfR1-mediated transport across the BBB, while non-functionalized CPNs fail to achieve detectable cerebral deposition under identical conditions. Together, these findings confirm that holo-Tf bioconjugation not only enhances targeting in vitro but also improves in vivo delivery to the central nervous system without altering the canonical reticuloendothelial clearance profile of the formulation.

We assessed the antitumor efficacy of systemically administered F8BT-PtOEP-Tf CPNs and F8BT-PtOEP CPNs ($1\ mg\cdot kg^{-1}$ i.v.) in our orthotopic U87MG-tdiRFP GBM model (n = 6 mice per group). Ten days after stereotactic implantation, animals were randomized to six arms: untreated control, light only, F8BT-PtOEP CPNs (no light), F8BT-PtOEP CPNs + light, F8BT-PtOEP-Tf CPNs (no light) and F8BT-PtOEP-Tf CPNs + light. A modest cranial trepanation was performed at the implant site to provide efficient brain lighting, followed by the delivery of fiber-optic LED illumination ($20\ mW\cdot cm^{-2}$ at the fiber tip, 10 min; total fluence $12\ J\cdot cm^{-2}$) 24 hours post-nanoparticle administration. Tumor size was evaluated ex vivo by NIR fluorescence (tdiRFP) at the humane endpoint, and overall survival was recorded as the primary efficacy endpoint. Ex vivo NIR imaging of excised brains demonstrated notable differences between treatment groups (Figure 6C). Brains from mice treated with F8BT-PtOEP-Tf CPNs followed by light displayed markedly lower integrated tumor fluorescence compared with untreated controls and with CPNs administered without subsequent illumination. The light-only group and the non-irradiated nanoparticle groups exhibited fluorescence signals comparable to controls, indicating minimal antitumor effect in the absence of combined nanoparticle delivery and photostimulation. Quantification of the tumor region of interest confirmed the visual impression: animals receiving holo-Tf-decorated CPNs followed by illumination had the lowest mean fluorescence intensities among the groups (Figure 6D).

Consistent with the imaging findings, survival analysis revealed treatment-dependent differences in median survival. Animals treated with F8BT-PtOEP-Tf CPNs plus light showed the most pronounced prolongation of survival relative to controls, while F8BT-PtOEP CPNs + light produced a more modest benefit. Groups that received CPNs without illumination or light alone showed no appreciable improvement in survival compared with untreated animals. Kaplan–Meier analysis and pairwise comparisons were performed (Log rank test; see Methods), and the F8BT-PtOEP-Tf CPNs + light group exhibited the largest therapeutic effect (Figure 6E).

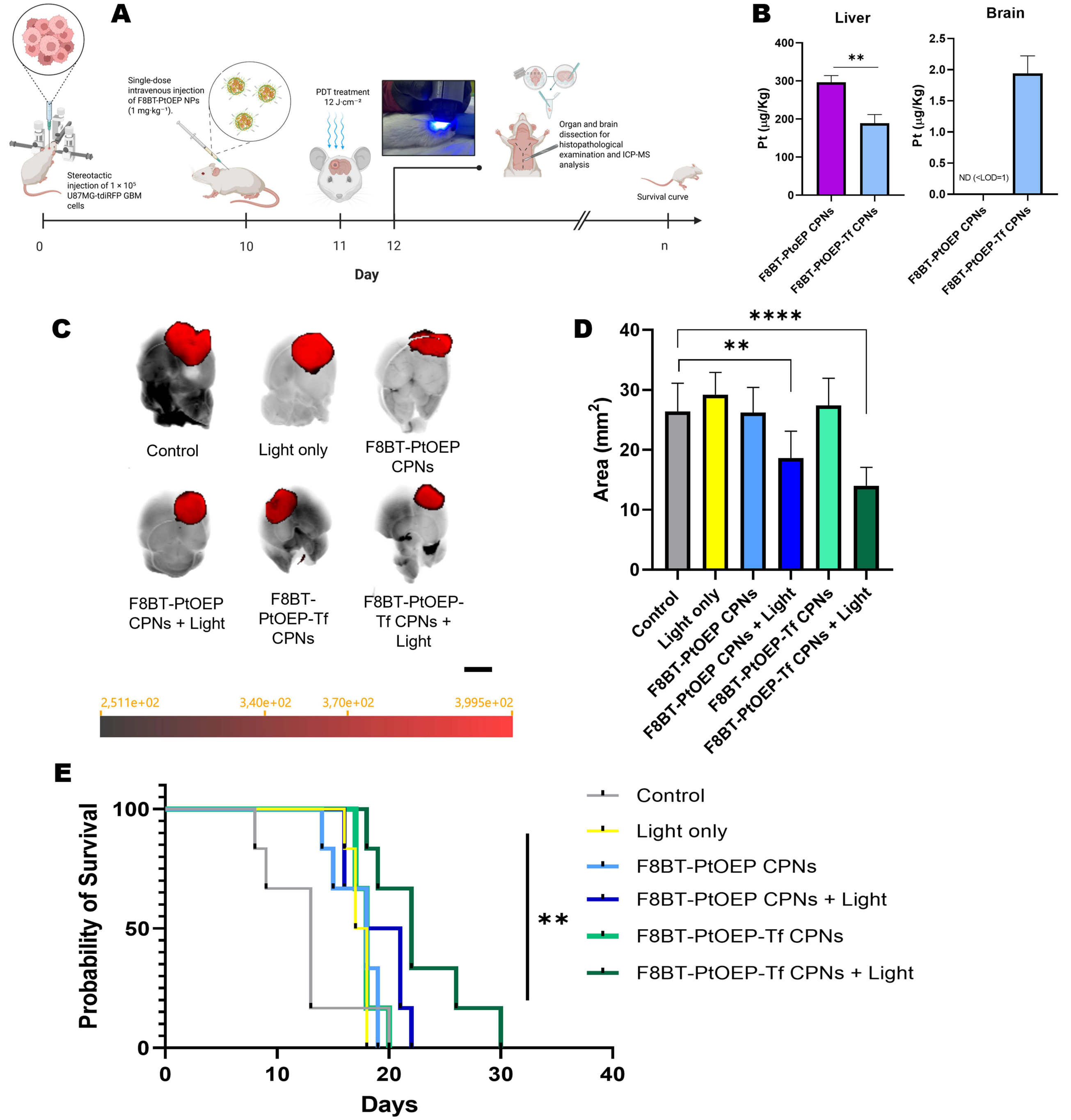

Figure 6 In vivo therapeutic evaluation, biodistribution, and experimental workflow of F8BT-PtOEP CPNs with and without holo-Tf in an orthotopic U87MG-tdiRFP GBM model. (**A**) Schematic overview of the experimental design. U87MG-tdiRFP cells were stereotactically implanted on day 0. Nanoparticle formulations (1 mg·kg^{-1}, i.v.) were administered on day 10, and PDT was applied 24 h later (day 11). Illumination was delivered through a minimal cranial trepanation using a fiber-optic LED source (irradiance 20 mW·cm^{-2} at the fiber tip, 10 min; total fluence 12 J·cm^{-2}) and was delivered through a minimal cranial trepanation created at the tumor implantation site to allow direct transmission of light into the brain parenchyma while minimizing attenuation by the skull. Animals were subsequently monitored for survival. (**B**) Biodistribution of Pt-containing CPNs 24 h after systemic administration in tumor-bearing mice (n = 4 per group). Platinum levels were quantified by ICP-MS. Both formulations showed predominant hepatic accumulation, consistent with reticuloendothelial clearance of polymeric nanoparticles. Detectable Pt levels in brain tissue were observed only in the F8BT-PtOEP-Tf CPNs group, whereas Pt concentrations in mice receiving F8BT-PtOEP CPNs remained below the analytical limit of detection (LOD = 1 ppb). (**C**) Representative ex vivo NIR fluorescence images of excised brains collected at humane endpoint. Tumor burden derived from the tdiRFP reporter is shown in pseudocolor (red) over a grayscale anatomical background. Images were acquired under identical imaging conditions and correspond to the following experimental groups (displayed uniformly across panels): Control, Light only, F8BT-PtOEP CPNs, F8BT-PtOEP CPNs + Light, F8BT-PtOEP-Tf CPNs, and F8BT-PtOEP-Tf CPNs + Light. Fluorescence intensity scale is shown below. Scale bar = 5 mm. (**D**) Quantification of ex vivo tumor fluorescence area (mean ± SD, n = 4 per group), demonstrating the greatest reduction in tumor signal in animals treated with F8BT-PtOEP-Tf CPNs followed by light irradiation. (**E**) Kaplan–Meier survival analysis for all treatment groups (n = 6 per group). The F8BT-PtOEP-Tf CPNs + Light group showed the most pronounced survival benefit, followed by the F8BT-PtOEP CPNs + Light group, whereas nanoparticle-only and light-only controls produced no significant improvement. Statistical significance was evaluated using the log-rank (Mantel–Cox) test. **$p < 0.01$, ****$p < 0.0001$. Illustrations created with BioRender.

https://doi.org/10.2147/IJN.S592688

Collectively, our findings suggest that the systemic administration of PtOEP-doped CPNs alone is unable to impede the growth of intracranial U87MG tumors, while light exposure without the presence of nanoparticle photosensitizers has minimal impact. The combination of holo-Tf functionalization with light activation produces the most significant antitumor response in this animal. The higher effectiveness of the holo-Tf–decorated formulation aligns with greater tumor targeting and cellular absorption through TfR-mediated mechanisms, therefore augmenting the local phototoxic payload for PDT. Histopathological and biodistribution analyses are necessary to elucidate the processes responsible for the enhanced therapeutic index and to assess off-target accumulation and safety.

Histopathological Correlations of PDT Response

Histopathological analysis of brain sections collected at the humane endpoint (n = 4 per group) revealed distinct morphological patterns associated with each treatment condition (Figure 7). Untreated control tumors exhibited features consistent with aggressive GBM, with a compact cellular arrangement and densely packed sheets of neoplastic cells. Tumors displayed prominent vascular structures with irregular profiles, consistent with active angiogenic remodeling. Neoplastic cells demonstrated moderate-to-marked pleomorphism and frequent mitotic activity (20 mitoses per 2.37 mm^2), with no evidence of extensive necrotic areas.

In the irradiated-only control group, GBM maintained an expansive and infiltrative growth pattern. Cellular proliferation was observed extending irregularly into the adjacent brain parenchyma, without evidence of a fibrous capsule or a well-defined boundary delimiting the lesion. Neoplastic cells appeared interdigitated with the surrounding neuropil and native brain structures, accompanied by loss of normal tissue architecture. These morphological features are consistent with the infiltrative growth pattern characteristic of diffuse gliomas as described in the literature. High cellular density and marked nuclear pleomorphism were observed, accompanied by frequent mitoses (15 mitoses per 2.37 mm^2). Necrosis with palisading-like arrangements was present, together with endothelial proliferation and irregular vascular morphologies, indicative of persistent tumor-associated angiogenic activity.[30–32]

Brain tissue from animals treated with F8BT-PtOEP CPNs or F8BT-PtOEP-Tf CPNs without irradiation showed tumor regions interspersed with areas of partially preserved parenchyma without clearly defined tumor boundaries. Neoplastic cells were observed extending between existing tissue structures, progressively obscuring tissue boundaries. Cells exhibited hyperchromatic nuclei, pleomorphism, and mitotic figures (18 mitoses per 2.37 mm^2). Irregular vascular profiles were evident within the tumor stroma.

Following PDT with non-functionalized F8BT-PtOEP CPNs, tumors displayed clear treatment-associated morphological alterations. Wide regions of coagulative necrosis and large hemorrhagic foci occupied significant portions of the tumor mass. Tumor-associated vasculature appeared irregular and frequently dilated, with morphological features suggestive of vascular injury. Tumor cellularity was reduced, and mitotic activity was lower than in non-irradiated groups. Dark granular pigment deposits, compatible with hemoglobin breakdown products, were found in tumoral and perivascular regions, reflecting hemorrhagic processes.

The most pronounced histopathological alterations were observed in the PDT-treated F8BT-PtOEP-Tf CPNs group. Tumors demonstrated a markedly disrupted and loose architecture, lacking the compact arrangement typical of untreated lesions. Extensive coagulative necrosis and widespread hemorrhage were present throughout the tumor. Neoplastic cells appeared sparsely distributed among damaged areas, and tumor vasculature showed severe structural alterations. Mitotic figures were markedly reduced (8 mitoses per 2.37 mm^2). Numerous cells displayed morphological features consistent with cell death, including pyknosis and apoptotic-like profiles. These findings support enhanced therapeutic efficacy when holo-Tf was used to facilitate receptor-mediated nanoparticle uptake. The data collectively indicates that PDT facilitated by F8BT-PtOEP CPNs results in significant tumor elimination in vivo, with this effect markedly intensified when NPs are functionalized with holo-Tf, aligning with improved intratumoral delivery and cytotoxic response.

These morphological observations are consistent with well-established histopathological features of GBM, including high cellularity, nuclear pleomorphism, vascular abnormalities, and necrotic regions associated with aggressive tumor growth and vascular remodeling.[33,34]

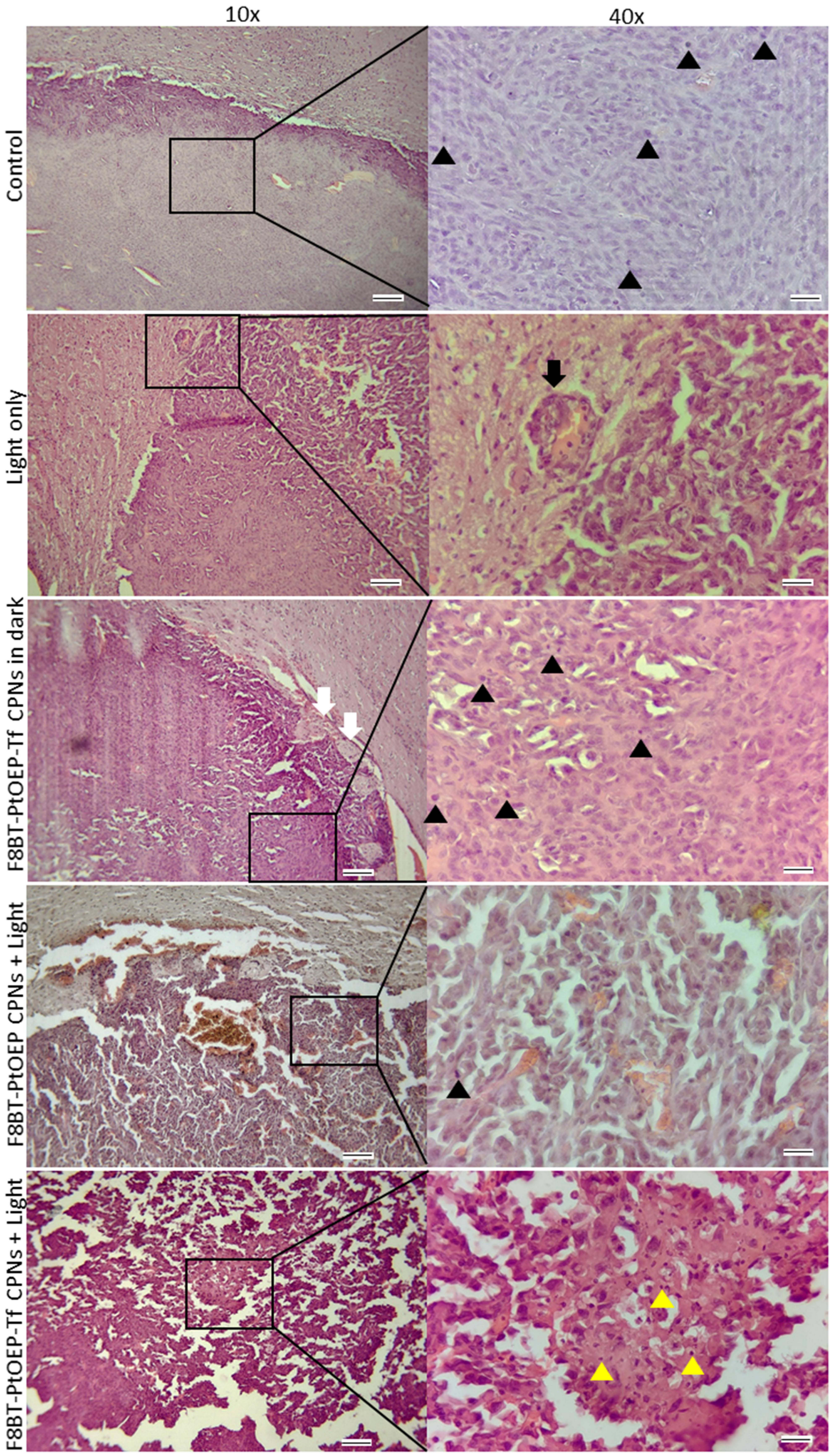

Figure 7 Histopathological evaluation of orthotopic U87MG-tdiRFP GBM following CPNs treatment and PDT. Representative hematoxylin–eosin–stained brain sections from each experimental group (n = 4) are shown, highlighting key morphological features associated with treatment response. Control tumors exhibit compact, highly cellular GBM architecture with moderate–marked pleomorphism and abundant blood vessels (black arrowheads: mitotic figures). Light-only controls display diffuse infiltration into adjacent parenchyma and neoformed aberrant vasculature (black arrow: perivascular neoplastic cells infiltrating into the brain parenchyma. The absence of a boundary with normal tissue is noted). In the non-irradiated F8BT-PtOEP-Tf CPNs -treated group, regions of partially preserved parenchyma are interspersed with infiltrating tumor cells (white arrows). GBM treated with non-functionalized F8BT-PtOEP CPNs + PDT shows extensive coagulative necrosis and hemorrhage, irregular hyperemic vessels, and palisading tumor-cell arrangements. The F8BT-PtOEP-Tf CPNs + PDT group demonstrates the most severe tissue disruption, with widespread necrosis, hemorrhage, and marked vascular damage, together with reduced mitotic activity and abundant cell death (yellow arrowhead: pyknosis). Scale bars = 100 (10x magnification) and 50 µm (40x magnification). The non-irradiated F8BT-PtOEP CPNs group is not shown for clarity, as its histological features were comparable to those observed in the other nanoparticle-treated group under dark conditions.

https://doi.org/10.2147/IJN.S592688

Discussion

In this study we engineered holo-Tf-functionalized CPNs based on F8BT doped with PtOEP as a theranostic platform for GBM PDT. Functionalization produced stable protein decoration, enhanced uptake in TfR-high GBM cells, and improved PDT efficacy both in vitro and in an orthotopic U87MG-tdiRFP model, supporting the concept that receptor-targeted CPNs increase tumor selectivity and local phototoxic payload.

Physicochemical and optical characterization confirmed that holo-Tf functionalization does not compromise the photophysical integrity of the F8BT core while providing clear surface modification signatures. The complementary measurements and TEM observations provide robust evidence of successful conjugation and an intact polymeric core after modification. The electrophoretic mobility and fluorescamine assays further corroborate covalent protein attachment rather than simple adsorption. Maintaining the core optical properties after conjugation is critical for a theranostic platform where imaging and singlet-oxygen production are both required; our results indicate that holo-Tf decoration can be achieved without deleterious quenching of the CP singlet excited state.

Mechanistically, the improved biological performance of holo-Tf-decorated CPNs is supported by in silico and flow-cytometry data showing elevated TFRC/TfR1 expression in GBM and in the U87MG model, and by competition experiments demonstrating that excess free holo-Tf markedly reduces cellular uptake of holo-Tf-CPNs. The strong reduction of gMFI and percentage-positive cells upon competition argues for a predominant contribution of TfR-mediated endocytosis to the enhanced internalization; the residual uptake after competition indicates concurrent TfR-independent pathways (eg, macropinocytosis, passive adsorption) that likely contribute to baseline nanoparticle accumulation. Confocal imaging reinforced these conclusions by revealing increased punctate, intracellular nanoparticle signal and more uniform cytoplasmic distribution after holo-Tf functionalization. Collectively, these data support the working model that holo-Tf increases receptor-dependent binding and internalization, thereby concentrating the PS within tumor cells. These findings are concordant with reports by Sun et al, who developed holo-Tf-conjugated F8BT nanoparticles and documented a marked enhancement of receptor-mediated uptake in cervical cancer cells. In that study, holo-Tf conjugation increased endocytic efficiency by approximately 67.5% in HeLa cells, underscoring the high affinity of the Tf–TfR1 interaction and the utility of Tf as a targeting ligand for nanoparticle delivery.[35]

The improved targeting translated into enhanced PDT efficacy. In vitro experiments showed that holo-Tf functionalization significantly reduced the IC_{50} in TfR-high U87MG cells, while the effect was less pronounced in the TfR-low T98G line, highlighting the dependence of ligand-directed nanomedicines on target expression. Similar studies have demonstrated that holo-Tf-targeted nanocarriers exploit TfR1 overexpression to enhance tumor uptake and therapeutic performance.[29] Consistent with these observations, nanoparticles functionalized with holo-Tf have been reported to exhibit preferential uptake and enhanced photodynamic activity in tumor cells compared with non-functionalized formulations.[36] Conversely, although only a few studies have explored the conjugation of CPNs with holo-Tf to improve tumor cell labeling,[35,37] to date there has been no demonstration of improved irradiation-mediated therapeutic efficacy using these systems.

In the orthotopic U87MG-tdiRFP model, systemic administration of PtOEP-F8BT-Tf CPNs followed by cranial illumination produced the most marked reductions in ex vivo tumor fluorescence and the largest extension in survival compared with non-functionalized CPNs or light alone. These in vivo data establish proof-of-concept that receptor targeting can improve therapeutic index in intracranial disease.

Biodistribution analysis showed predominant accumulation of both targeted and non-targeted CPNs in liver and spleen, consistent with clearance by the mononuclear phagocyte system.[15] Holo-Tf functionalization slightly reduced the total Pt recovered from peripheral organs, possibly reflecting altered nanoparticle hydrodynamics and protein corona effects that influence macrophage recognition and systemic clearance.

Notably, the total Pt recovered from peripheral organs was slightly lower in the PtOEP-F8BT-Tf CPNs group compared with its non-functionalized counterpart. Although mechanistic interpretation remains speculative, this modest reduction in systemic burden may reflect changes in hydrodynamic behavior arising from the holo-Tf protein corona, potentially enhancing hepatosplenic uptake and accelerating systemic clearance. These trends align with previous reports describing how protein-functionalized nanocarriers exhibit modified serum stability, altered macrophage recognition, and distinct pharmacokinetic profiles relative to their non-coated analogues.[38–40]

Importantly, while holo-Tf decoration enabled quantifiable nanoparticle deposition in the brain, Pt levels in the PtOEP-F8BT CPNs group fell below the ICP-MS detection limit (<1 ppb). This analytical limitation should not be interpreted as complete absence of nanoparticles from the orthotopic tumor. Several methodological factors likely contributed to this observation. First, the ICP-MS analysis quantified platinum derived from PtOEP, which represents only a minor component of CPNs. Second, measurements were performed on whole brain tissue, which may dilute the signal originating from the tumor region. In orthotopic GBM models, tumors are typically small and highly infiltrative, making precise microdissection of tumor tissue for elemental analysis technically challenging. Consequently, even limited nanoparticle accumulation within the tumor may remain below the quantitative detection threshold of the Pt-based assay. Previous work from our group using compositionally related CPNs containing iron oxide cores demonstrated intratumoral nanoparticle accumulation detectable by MRI, even in the absence of active targeting.[41] These findings are consistent with the heterogeneous disruption of the BBB commonly observed in GBM and support the interpretation that a fraction of non-targeted PtOEP-F8BT CPNs likely reached the tumor microenvironment despite remaining below the analytical detection limit of ICP-MS.

Taken together, these considerations indicate that ICP-MS measurements performed on whole brain tissue may underestimate the true nanoparticle concentration within the tumor microenvironment, where BBB permeability is heterogeneous. Despite this limitation, two key conclusions emerge from our data. First, holo-Tf functionalization enhances brain delivery through TfR1-mediated transcytosis, enabling measurable nanoparticle accumulation in brain tissue. Second, the lack of detectable Pt in the non-targeted group likely reflects analytical sensitivity and tissue dilution rather than complete absence of nanoparticles, as supported by the observed PDT-induced tumor damage. These findings suggest that both targeted and untargeted CPNs are capable of crossing the BBB to some extent, while holo-Tf functionalization markedly improves delivery efficiency, consistency, and therapeutic potential.

Several limitations should be acknowledged. The orthotopic efficacy experiment required cranial trepanation and fiber-optic illumination, which, although appropriate for preclinical proof-of-concept, does not fully reflect clinical PDT procedures. In addition, the U87MG xenograft model in NOD-SCID mice lacks an intact immune system, preventing evaluation of immune-mediated PDT effects. From a materials perspective, the photodynamic activity of these systems arises from the combined contribution of the light-harvesting properties of the F8BT polymer matrix and the singlet oxygen quantum yield (ΦΔ) of the PtOEP dopant, where F8BT acts as an antenna that efficiently transfers excitation energy to PtOEP. Under these conditions, increasing the PtOEP content is not expected to proportionally enhance singlet oxygen generation, as the excited states of F8BT are already effectively quenched by the dopant. Nevertheless, the relatively low Pt content may limit the sensitivity of elemental quantification in biodistribution studies. Furthermore, interactions with serum proteins and the formation of a protein corona can influence nanoparticle biodistribution, clearance, and targeting efficiency. Another important consideration is that CPNs such as those based on F8BT exhibit very limited intrinsic biodegradability, which may lead to prolonged persistence in tissues and highlight the need for comprehensive long-term pharmacokinetic and safety studies. Further investigations will therefore be required to evaluate biodistribution and clearance in immunocompetent and patient-derived glioma models, as well as to optimize nanoparticle formulation, ligand density, and illumination parameters.[42]

Despite these limitations, the present results demonstrate that holo-Tf functionalization significantly enhances the delivery and photodynamic performance of CPNs in GBM models. These findings support the continued development of receptor-targeted CPN platforms as a promising strategy to improve the selectivity and therapeutic efficacy of PDT in brain tumors.

Conclusion

We report that covalent functionalization of F8BT-PtOEP NPs with holo-Tf produces a reproducible surface modification that preserves the photophysical integrity of the CP core; slightly increases nanoparticle hydrodynamic size and reduces the magnitude of negative surface charge consistent with a protein corona and substantially enhances receptor-mediated uptake in TfR-expressing GBM models. Functionally, holo-Tf-decorated CPNs delivered a larger intracellular PS payload and produced greater phototoxicity in vitro and superior antitumor effects in an orthotopic U87MG xenograft model following systemic administration and localized cranial illumination.

These results validate the central concept that TfR-directed CPNs can improve tumor selectivity and the local therapeutic index of PDT in intracranial disease. Importantly, enhanced targeting was achieved under serum-containing conditions, indicating that the holo-Tf ligand retains functional accessibility for receptor engagement despite potential biomolecular corona formation. The platform therefore offers an integrated theranostic advantage, combining targeted delivery, retained fluorescence for imaging, and a PS activity for light-activated cytotoxicity.

In summary, holo-Tf functionalization significantly increases receptor-targeted delivery and therapeutic efficacy of F8BT-PtOEP CPNs in GBM models while preserving key optical properties required for theranostic applications. These findings support continued preclinical development and provide a clear roadmap of experimental and translational milestones necessary to advance TfR-targeted CPN-based PDT toward early-phase clinical evaluation.

Data Sharing Statement

The datasets used and/or analysed during the current study are available from the corresponding author on reasonable request.

Acknowledgments

The authors express their gratitude to the authorities of JLA Argentina SA (JLA.com.ar, accessed on 20 October 2025) for their invaluable contribution in conducting IPC-MS analysis at no cost. In particular, we thank Naara Chiappero for sample handling and evaluation and Ivan Cabanillas for his instrumental role in facilitating the collaboration.

Matias D. Caverzan and Bruno A. Cesca thank CONICET for Ph. D. scholarships. C.A.C., R.E.P. and L.E.I. are members of the Scientific Researcher Career at CONICET and faculty at UNRC.

Funding

This work was supported by the SECyT UNRC (PPI 2024), ANPCyT (PICT 2020/51; 2020/3803), CONICET (PIP 11220200102377CO01) to L.E.I., C.A.C. and R.E.P.

Disclosure

The author(s) report no conflicts of interest in this work.

References

1. Lakomy R, Kazda T, Selingerova I, et al. Real-world evidence in glioblastoma: Stupp's Regimen after a decade. *Front Oncol*. 2020;10:840. doi:10.3389/FONC.2020.00840/BIBTEX
2. Skaga E, Kulesskiy E, Fayzullin A, et al. Intertumoral heterogeneity in patient-specific drug sensitivities in treatment-naïve glioblastoma. *BMC Cancer*. 2019;19(1):628. doi:10.1186/s12885-019-5861-4
3. Cesca BA, Pellicer K, Martin S, Caverzan MD, Oliveda PM, Ibarra LE. State-of-the-art photodynamic therapy for malignant gliomas: innovations in photosensitizers and combined therapeutic approaches. *Explor Target Antitumor Ther*. 2025;6:1002303. doi:10.37349/ETAT.2025.1002303
4. Ibarra LE, Vilchez ML, Caverzán MD, Milla Sanabria LN. Understanding the glioblastoma tumor biology to optimize photodynamic therapy: from molecular to cellular events. *J Neurosci Res*. 2021;99(4):1024–1047. doi:10.1002/jnr.24776
5. Zhang J, Yan X, Gao X, et al. Three decades of photodynamic therapy for glioblastoma: a comprehensive scientometric analysis. *Photodiagnosis Photodyn Ther*. 2025;53:104533. doi:10.1016/J.PDPDT.2025.104533
6. Hsia T, Small JL, Yekula A, et al. Systematic review of photodynamic therapy in gliomas. *Cancers*. 2023;15(15):3918. doi:10.3390/CANCERS15153918
7. Bhanja D, Wilding H, Baroz A, et al. Photodynamic therapy for glioblastoma: illuminating the path toward clinical applicability. *Cancers*. 2023;15(13):3427. doi:10.3390/CANCERS15133427
8. Ibarra LE, Porcal G, Macor LP, et al. Metallated porphyrin doped conjugated polymer nanoparticles for efficient PDT of brain and colorectal tumor cells. *Nanomedicine*. 2018;13(6):605–624. doi:10.2217/nnm-2017-0292
9. Caverzán MD, Beaugé L, Chesta CA, Palacios RE, Ibarra LE. Photodynamic therapy of Glioblastoma cells using doped conjugated polymer nanoparticles: an in vitro comparative study based on redox status. *J Photochem Photobiol B*. 2020;212:112045. doi:10.1016/j.jphotobiol.2020.112045
10. Spada RM, Macor LP, Hernández LI, et al. Amplified singlet oxygen generation in metallated-porphyrin doped conjugated polymer nanoparticles. *Dyes Pigm*. 2018;149:212–223. doi:10.1016/j.dyepig.2017.09.044
11. Aebisher D, Szpara J, Bartusik-Aebisher D. Advances in medicine: photodynamic therapy. *Int J Mol Sci*. 2024;25(15):8258. doi:10.3390/IJMS25158258
12. Ibarra LE, Camorani S, Agnello L, et al. Selective photo-assisted eradication of triple-negative breast cancer cells through aptamer decoration of doped conjugated polymer nanoparticles. *Pharmaceutics*. 2022;14(3):626. doi:10.3390/pharmaceutics14030626

13. Modicano P, Trutschel ML, Phan-Xuan T, et al. Does encapsulation of π-conjugated polymer nanoparticles within biodegradable PEG–PLGA matrices mitigate photoinduced free radical production and phototoxicity? *Adv Ther*. 2025;8(1):2400190. doi:10.1002/ADTP.202400190
14. Elgiddawy N, Elnagar N, Korri-Youssoufi H, Yassar A. π-conjugated polymer nanoparticles from design, synthesis to biomedical applications: sensing, imaging, and therapy. *Microorganisms*. 2023;11(8):2006. doi:10.3390/microorganisms11082006
15. Caverzan MD, Belén A, Vasconsuelo M, et al. Preclinical toxicological characterization of porphyrin-doped conjugated polymer nanoparticles for photodynamic therapy. *Pharmaceutics*. 2025;17(5):593. doi:10.3390/PHARMACEUTICS17050593
16. Tai SSA, Loo HL, Bakhtiar A, Ho PCL, Chuah LH. Antibody-conjugated polymer nanoparticles for brain cancer. *Drug Deliv Transl Res*. 2025;15 (11):4367–4410. doi:10.1007/S13346-025-01947-0/FIGURES/2
17. Nguyen LNM, Ngo W, Lin ZP, et al. The mechanisms of nanoparticle delivery to solid tumours. *Nat Rev Bioeng*. 2024;2(3):201–213. doi:10.1038/s44222-024-00154-9
18. Caverzan MD, Ibarra LE. Advancing glioblastoma treatment through iron metabolism: a focus on TfR1 and ferroptosis innovations. *Int J Biol Macromol*. 2024;278:134777. doi:10.1016/J.IJBIOMAC.2024.134777
19. Ramalho MJ, Loureiro JA, Coelho MAN, Pereira MC. Transferrin receptor-targeted nanocarriers: overcoming barriers to treat glioblastoma. *Pharmaceutics*. 2022;14(2):279. doi:10.3390/PHARMACEUTICS14020279
20. Ni XR, Zhao YY, Cai HP, et al. Transferrin receptor 1 targeted optical imaging for identifying glioma margin in mouse models. *J Neurooncol*. 2020;148(2):245–258. doi:10.1007/s11060-020-03527-3
21. Rosager AM, Sørensen MD, Dahlrot RH, et al. Transferrin receptor-1 and ferritin heavy and light chains in astrocytic brain tumors: expression and prognostic value. *PLoS One*. 2017;12(8):e0182954. doi:10.1371/JOURNAL.PONE.0182954
22. Zhao X, He J, Chen Y, et al. Transferrin receptor-targeted aptamer–drug conjugate overcomes blood–brain barrier for potent glioblastoma therapy. *Bioconjug Chem*. 2025;36(6):1288–1298. doi:10.1021/ACS.BIOCONJCHEM.5C00137
23. Wang D, Liu J, Liu Z, et al. Bioconjugation of IgG secondary antibodies to polymer dots for multicolor subcellular imaging. *ACS Appl Nano Mater*. 2020;3(3):2214–2220. doi:10.1021/acsanm.9b02292
24. Choudhury H, Pandey M, Chin PX, et al. Transferrin receptors-targeting nanocarriers for efficient targeted delivery and transcytosis of drugs into the brain tumors: a review of recent advancements and emerging trends. *Drug Deliv Transl Res*. 2018;8(5):1545–1563. doi:10.1007/s13346-018-0552-2
25. Gao Y, Kyratzis I. Covalent immobilization of proteins on carbon nanotubes using the cross-linker 1-ethyl-3-(3-dimethylaminopropyl)carbodiimide - A critical assessment. *Bioconjug Chem*. 2008;19(10):1945–1950. doi:10.1021/BC800051C/ASSET/IMAGES/LARGE/BC-2008-00051C_0001.JPEG
26. Kabiri M, Amiri-Tehranizadeh Z, Baratian A, Saberi MR, Chamani J. Use of spectroscopic, zeta potential and molecular dynamic techniques to study the interaction between human holo-transferrin and two antagonist drugs: comparison of binary and ternary systems. *Molecules*. 2012;17:3114–3147. doi:10.3390/molecules17033114
27. Lu S, Khan MA, Setua S, et al. Transferrin Purification, Biophysical Characterization, and Lung Biodistribution in Sickle Cell Disease Mice. *Biotechnol Bioeng*. 2025;122(10):2709–2723. doi:10.1002/BIT.70012;WEBSITE:WEBSITE:ANALYTICALSCIENCEJOURNALS;ISSUE:ISSUE:DOI
28. Pace CN, Vajdos F, Fee L, Grimsley G, Gray T. How to measure and predict the molar absorption coefficient of a protein. *Protein Sci*. 1995;4 (11):2411–2423. doi:10.1002/PRO.5560041120
29. Li H, Sun H, Qian ZM. The role of the transferrin-transferrin-receptor system in drug delivery and targeting. *Trends Pharmacol Sci*. 2002;23 (5):206–209. doi:10.1016/S0165-6147(02)01989-2
30. Edalat L, Stegen B, Klumpp L, et al. BK K+ channel blockade inhibits radiationinduced migration/brain infiltration of glioblastoma cells. *Oncotarget*. 2016;7(12):14259–14278. doi:10.18632/ONCOTARGET.7423
31. Palfi S, Swanson KR, De Boüard S, et al. Correlation of in vitro infiltration with glioma histological type in organotypic brain slices. *Br J Cancer*. 2004;91(4):745–752. doi:10.1038/sj.bjc.6602048
32. Perry A, Wesseling P. Histologic classification of gliomas. *Handb Clin Neurol*. 2016;134:71–95. doi:10.1016/B978-0-12-802997-8.00005-0
33. Candolfi M, Curtin JF, Nichols WS, et al. Intracranial glioblastoma models in preclinical neuro-oncology: neuropathological characterization and tumor progression. *J Neuro-oncol*. 2007;85(2):133–148. doi:10.1007/S11060-007-9400-9
34. Brighi C, Reid L, Genovesi LA, et al. Comparative study of preclinical mouse models of high-grade glioma for nanomedicine research: the importance of reproducing blood-brain barrier heterogeneity. *Theranostics*. 2020;10(14):6361–6371. doi:10.7150/THNO.46468
35. Sun Z, Yuan Y, Li Q, Liu Z, Wu C. Imaging fast cellular uptake of polymer dots via receptor-mediated endocytosis. *J Anal Test*. 2018;2(1):61–68. doi:10.1007/s41664-018-0048-6
36. Gvozdev DA, Ramonova AA, Slonimskiy YB, Maksimov EG, Moisenovich MM, Paschenko VZ. Modification by transferrin increases the efficiency of delivery and the photodynamic effect of the quantum dot–phthalocyanine complex on A431 cells. *Arch Biochem Biophys*. 2019;678:108192. doi:10.1016/J.ABB.2019.108192
37. Yu N, Wang Y, Xia J, Abashkin V, Zhao L, Li J. Transferrin-conjugated manganese dioxide/semiconducting polymer hybrid nanoparticles for targeted dual-model imaging of orthotopic glioblastoma. *ACS Appl Polym Mater*. 2023;5(6):4596–4603. doi:10.1021/ACSAPM.3C00881
38. Ernsting MJ, Murakami M, Roy A, Li SD. Factors controlling the pharmacokinetics, biodistribution and intratumoral penetration of nanoparticles. *J Control Release*. 2013;172(3):782–794. doi:10.1016/J.JCONREL.2013.09.013
39. Papini E, Tavano R, Mancin F. Opsonins and dysopsonins of nanoparticles: facts, concepts, and methodological guidelines. *Front Immunol*. 2020;11:567365. doi:10.3389/FIMMU.2020.567365/BIBTEX
40. Suvarna M, Dyawanapelly S, Kansara B, Dandekar P, Jain R. Understanding the stability of nanoparticle–protein interactions: effect of particle size on adsorption, conformation and thermodynamic properties of serum albumin proteins. *ACS Appl Nano Mater*. 2018;1(10):5524–5535. doi:10.1021/ACSANM.8B01019
41. Arias-Ramos N, Ibarra LE, Serrano-Torres M, et al. Iron oxide incorporated conjugated polymer nanoparticles for simultaneous use in magnetic resonance and fluorescent imaging of brain tumors. *Pharmaceutics*. 2021;13(8):1258. doi:10.3390/pharmaceutics13081258
42. Caverzán MD, Oliveda PM, Beaugé L, Palacios RE, Chesta CA, Ibarra LE. Metronomic photodynamic therapy with conjugated polymer nanoparticles in glioblastoma tumor microenvironment. *Cells*. 2023;12(11):1541. doi:10.3390/cells12111541